

Article

Quantum Finite-Time Thermodynamics: Insight from a Single Qubit Engine

Roie Dann ^{1,*}, Ronnie Kosloff ¹  and Peter Salamon ² 

¹ The Institute of Chemistry, The Hebrew University of Jerusalem, Jerusalem 9190401, Israel; ronnie@fh.huji.ac.il

² Department of Mathematics and Statistics, San Diego State University, 5500 Campanile Drive, San Diego, CA 92182-7720, USA; salamon@sdsu.edu

* Correspondence: roie.dann@mail.huji.ac.il

Received: 6 September 2020; Accepted: 1 November 2020; Published: 4 November 2020



Abstract: Incorporating time into thermodynamics allows for addressing the tradeoff between efficiency and power. A qubit engine serves as a toy model in order to study this tradeoff from first principles, based on the quantum theory of open systems. We study the quantum origin of irreversibility, originating from heat transport, quantum friction, and thermalization in the presence of external driving. We construct various finite-time engine cycles that are based on the Otto and Carnot templates. Our analysis highlights the role of coherence and the quantum origin of entropy production.

Keywords: finite-time thermodynamics; quantum thermodynamics; quantum heat engine; carnot cycle; otto cycle

1. Introduction

The tradeoff between power and efficiency is well embedded in our everyday experience. It is witnessed in the performance of any realistic engine or refrigerator, from the operation of large nuclear plants, through the internal combustion engines of our automobiles, and all the way to microscopic biological engines and the quantum regime. Despite the intuitive notion, a theoretical analysis is quite involved, as it requires a theoretical construction that encompasses both thermodynamics and transient dynamics.

The limiting case was first treated by Carnot, who linked an engine's maximum attainable work production to reversible thermodynamic transformations, thereby obtaining the thermodynamic temperature scale and the universal optimal efficiency that only depends on the hot and cold bath temperatures [1]. Unlike efficiency, power requires knowledge of the transient dynamics, which is outside the realm of classical thermodynamics. Finite-time thermodynamics (FTT) was developed in order to include the limitations the process duration places on the performance of an engine [2–6]. Originally, the pioneers of FTT incorporated empirical kinetic laws to introduce an intrinsic timescale in the analysis of engine cycles [7,8]. Some results from these efforts are recapped in Section 2.1. In this paper, we address the need for kinetic laws by following a different approach: building upon a complete quantum description of the engine and baths.

However, such complete quantum description is not as straightforward as it sounds. Quantum mechanics is a dynamical theory that can supply equations of motion for thermodynamic processes. The well established portion of this theory has predominantly dealt with closed systems that conserve entropy and, thus, cannot deal with dissipation phenomena at the heart of thermodynamic analyses. This forces us to turn to open quantum systems, whose description from first principles relies on a reduction from a closed composite system. The reduced description is achieved by tracing over the

degrees of freedom of the surroundings, interacting with our system of interest. This description does not conserve entropy and allows for the exploration of thermodynamic processes in the quantum regime. Notably, the approach is based on the completely positive trace preserving (CPTP) dynamical map [9] and the Markovian Gorini–Kossakowski–Lindblad–Sudarshan (GKLS) master equation [10,11]. A thermodynamically consistent dynamical framework [12] is obtained by a first principle derivation based on weak interaction of an open system with a heat bath. The derivation is commonly termed the ‘Davies construction’ [13].

The quantum open system approach resulted in a number of surprises, initially reported as claimed contradictions to the second law [14–19]. These include reported claims of breakdown of the Carnot bound in such engines [20–22]. In turn, these results led to resolutions, explained by unexpected work that is available from quantum resources, including coherence [23], squeezed bath [24], entanglement [25], and information [26,27].

Another set of surprises came from attempts to use a naive GKLS formalism with a time-dependent driving, which possibly violates the second law [28–31]. This led to the realization that the inconsistency arises from the derivation of the reduced dynamics of the system. For periodic driving, a thermodynamically consistent GKLS equation was derived in Ref. [32]. In the case of a general (non-periodic) driving, only the adiabatic master equation was available [33]. This fact did not limit the analysis of the Otto cycle model, which could be studied up to the limit of vanishing cycle times. On the contrary, the analysis of the Carnot cycle model was limited to the linear response regime. Only recently has a derivation of the GKLS master equation for rapid non-adiabatic driving become available [34], and it is this discovery whose implications we explore in the present paper.

We adopt the dogma that thermodynamics and quantum mechanics address the same subject matter, therefore have to be consistent [35]. In this framework, quantum mechanics provides the tools for describing the dynamics, while the strict laws of thermodynamics must be obeyed. In addition, recent progress in the theory of quantum speed limits can illuminate fundamental bounds on the process timescale [36–41].

Engines have been an intrinsic part in the development of classical thermodynamics. Their analysis still serves as an integral part of current research in finite-time and quantum thermodynamics. These theories allow for describing engines more realistically including non-ideal performance. Any practical engine operates in a non-ideal irreversible mode. Typically, there are four sources of irreversible phenomena in engines:

1. Finite heat transport.
2. Friction.
3. Heat leaks.
4. Cost of switching contacts between subsystems.

Following the thermodynamic tradition of learning from example, we employ the most elementary working medium, a spin one half system to explore a quantum version of finite-time thermodynamics. A decade ago, such an example would have been criticized as a theoretician’s toy with no connection to the world of real engines. The finite-time Otto type cycle, which our cars operate by, do not seem to be related to a single spin quantum engine. Nevertheless, recent experimental progress has enabled a realization of an Otto cycle engine constructed from a single spin of an atom in an ion trap [42], a single qubit in an impurity electron spin [43], or a working medium of ultracold hyperfine structure of Cs in a Rb bath [44].

The present paper begins by laying the quantum thermodynamic foundations for the qubit, giving the quantum definitions for energy, entropy, and temperature, Section 2.2. We continue by discussing sources of irreversibility: heat transport, Section 3, the quantum origin of friction, Section 4, and thermalization processes which combine heat transport and external work, Section 5. The quantum version of finite-time thermodynamics is studied by constructing two basic engine platforms: Carnot and Otto. These models illuminate different aspects of the tradeoff between power and efficiency and the role of coherence on the engines performance, Sections 6–8.

2. Some Preliminaries

The unfortunate collision of the different usages of the word adiabatic in thermodynamics and quantum mechanics have been sidestepped by using the term “unitary dynamics” for dynamics along what thermodynamics would call an adiabat leaving the use of adiabatic for the quantum meaning.

2.1. Classical Engines Operating in Finite-Time

Classical textbook treatments of heat engines define various kinds of engine cycles. These cycles are mostly four-stroke and consist of two unitary strokes and two open strokes in contact with a heat bath—one hot and one cold. Finite-time thermodynamic analyses of these cycles has given us the simplifying model of endoreversible processes—processes in which the participating systems are at each instant in equilibrium states and all irreversibility resides in the interactions between such systems. Endoreversible cycles play an important role by edging closer towards real cycles, being relatively easy to analyze and providing checks along the way for more ambitious treatments. They also provide an accurate picture of reality when the slow timescale is the interaction. The simplifying condition of instantaneous lossless adiabatic jumps, made possible for quantum systems using shortcuts to adiabaticity (cf. Section 4.3), is a hallmark simplifying feature that we inherit from these studies.

Additionally, important for these analyses is a much older result known as the Gouy—Stodola theorem [45–48] which established a connection between dissipated work and entropy production, cf.

$$\Delta\mathcal{A}^U = -T_0\Delta\mathcal{S}^U \quad (1)$$

where the superscript U refers to the universe (all participating systems), \mathcal{S} is the entropy, \mathcal{A} is the available work, and T_0 is the temperature at which heat is freely available which means it carries no available work. The environment temperature T_0 is also used in the availability (also called exergy) state function $\mathcal{A} = \mathcal{E} - T_0\mathcal{S}$, where \mathcal{E} is the internal energy. As a consequence, Equation (1) is valid with any constant temperature choice for T_0 . In engineering treatments it is always the atmospheric temperature, but any temperature will do. In the physics literature T_0 is almost always taken to be the system’s temperature making $\mathcal{A} = \mathcal{F}$, where \mathcal{F} is the Helmholtz free energy. Note that $\mathcal{A} = \mathcal{F}$ can hold at only one temperature.

For our purposes, the importance of Equation (1) arises from the fact that it shows that dissipation can equivalently be measured in energetic or entropic terms, even when the system does not have a temperature or when this temperature is changing during the process of interest.

2.2. Qubit Engine Model

The engine model is constructed from a hot and cold bath and a controllable two-level-system shuttling between them. The Hamiltonian of the working medium, a qubit, is

$$\hat{H} = \omega(t)\hat{S}_z + \epsilon(t)\hat{S}_x \quad (2)$$

where \hat{S}_j are the spin operators with the commutation relation of the $SU(2)$ algebra $[\hat{S}_i, \hat{S}_j] = i\hbar\epsilon_{ijk}\hat{S}_k$, see Appendix A. The time-dependent driving parameters $\omega(t)$ and $\epsilon(t)$, define a typical energy scale

$$\hbar\Omega(t) = \hbar\sqrt{\omega^2 + \epsilon^2} \quad , \quad (3)$$

where Ω is the Rabi frequency.

The state of the qubit working medium $\hat{\rho}$ can be expanded while using any orthonormal set of operators satisfying $\text{tr}\{\hat{A}_i^\dagger\hat{A}_j\} = \delta_{ij}$. Choosing the polarizations \hat{S}_j as basis operators, the state $\hat{\rho}$ is completely determined by the expectation value of the three polarizations

$$\hat{\rho} = \frac{1}{2}\hat{I} + \frac{2}{\hbar^2} (\langle\hat{S}_x\rangle\hat{S}_x + \langle\hat{S}_y\rangle\hat{S}_y + \langle\hat{S}_z\rangle\hat{S}_z) \quad . \quad (4)$$

It elucidates the analysis to represent the polarization vector as a geometric object $\vec{S} = \{\langle \hat{S}_x \rangle, \langle \hat{S}_y \rangle, \langle \hat{S}_z \rangle\}^T$, which resides inside the Bloch sphere (see Figure 1 and Appendix A). The polarization value is defined as

$$\bar{S} \equiv -|\vec{S}| = -\sqrt{\langle \hat{S}_x \rangle^2 + \langle \hat{S}_y \rangle^2 + \langle \hat{S}_z \rangle^2} . \tag{5}$$

It is related to the purity of the state, where $0 \geq \bar{S} \geq -\hbar/2$ where $|\vec{S}| = \hbar/2$ for a pure state. The sign convention of the polarization is motivated by the fact that we consider only positive temperatures, see Equation (6). The polarization value is invariant under unitary transformations that are generated by the $SU(2)$ group, which represents rotations of the polarization vector. It is related to the expectation value of the energy by $\mathcal{E} = \langle \hat{H} \rangle = \hbar\Omega\bar{S}_H$, where \bar{S}_H is the projection of the polarization vector on the direction representing the Hamiltonian. In thermal equilibrium at temperature T , the polarization becomes

$$\langle \vec{S} \rangle = \bar{S}_H = \bar{S}_{eq} = -\frac{\hbar}{2} \tanh\left(\frac{\hbar\Omega}{2k_B T}\right) , \tag{6}$$

where k_B is the Boltzmann constant and T is the bath temperature.

The engines that are to be analyzed are discrete four stroke cycle models. Specifically, we will compare the Carnot cycle with the Otto cycle. Both of the cycles are constructed from the following sequence of strokes:

- (A) 1 → 2 Hot bath thermalization.
- (B) 2 → 3 Unitary expansion from hot to cold
- (C) 3 → 4 Cold bath thermalization
- (D) 4 → 1 Unitary compression from cold to hot

The two cycles differ by the nature of the thermalization strokes, 1 → 2 and 3 → 4. The reversible Carnot cycle includes isothermal strokes during the thermalization processes, while the Otto cycle utilizes isochores, see Figure 2. In the following study, we sometimes refer to the thermalization strokes as open-strokes, alluding to the fact that the working medium constitutes an open quantum system during these strokes.

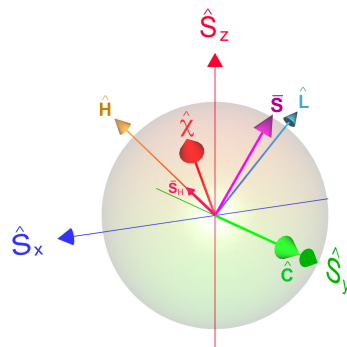


Figure 1. The state of the system, Equation (4), is represented by the polarization vector \vec{S} in the Bloch sphere (purple). Alternatively, the state can be represented in a rotated frame Equation (33), defined by the set of coordinates $\langle \hat{H} \rangle, \langle \hat{L} \rangle, \langle \hat{C} \rangle$ in Equation (32). These coordinates are rotated about the $\langle \hat{S}_y \rangle$ axis relative to the static direction. The projection of the polarization on the energy direction \bar{S}_H , Equation (13), is shown in light red. The invariant of the free propagator $\langle \hat{\chi} \rangle$ in Equation (52) is shown in red. The direction of $\langle \hat{\chi} \rangle$ is rotated around the $\langle \hat{L} \rangle$ axis with respect to the $\langle \hat{H} \rangle$ direction (cf. Appendix A). The Bloch sphere representation can represent either the expectation values of the operators or the operators themselves. The latter constitute orthogonal vectors in Liouville space.

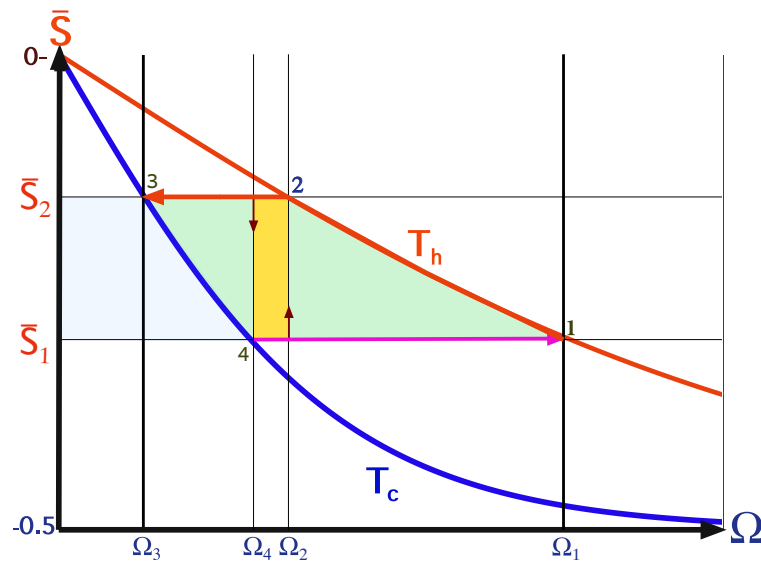


Figure 2. Carnot and Otto cycles: polarization \bar{S} as a function of frequency Ω is shown along the hot (red) and cold (blue) isotherms. The four switching points between the strokes are indicated by numbers 1–4. The various strokes are represented by lines. Carnot cycle: Hot isotherm $(\Omega_1, \bar{S}_1) \rightarrow (\Omega_2, \bar{S}_2)$, unitary expansion $(\Omega_2, \bar{S}_2) \rightarrow (\Omega_3, \bar{S}_2)$, cold isotherm $(\Omega_3, \bar{S}_2) \rightarrow (\Omega_4, \bar{S}_1)$, and unitary compression $(\Omega_4, \bar{S}_1) \rightarrow (\Omega_1, \bar{S}_1)$. The filled area in light green represents the work output, while the area in light blue represents the heat that is absorbed by the cold bath. The sum of the two areas equals the heat exchange with the hot bath. This implies a nice geometric representation of the efficiency, as the ratio between the light green area and the combined area. Otto cycle embedded in the Carnot cycle (orange area); hot isochore $(\Omega_2, \bar{S}_1) \rightarrow (\Omega_2, \bar{S}_2)$, unitary expansion $(\Omega_2, \bar{S}_2) \rightarrow (\Omega_4, \bar{S}_2)$, cold isochore $(\Omega_4, \bar{S}_2) \rightarrow (\Omega_4, \bar{S}_1)$, and unitary compression $(\Omega_4, \bar{S}_1) \rightarrow (\Omega_2, \bar{S}_1)$. The short arrows designate the thermalization isochores.

The four stroke cycles can be described by the corresponding cycle propagator Λ_{cyc} , which is a product of individual stroke propagators:

$$\Lambda_{cyc} = \Lambda_{c \rightarrow h} \Lambda_c \Lambda_{h \rightarrow c} \Lambda_h \tag{7}$$

These propagators are completely positive trace-preserving (CPTP) maps on the space of qubit states [9]. The properties of the engine are extracted from the fixed point of the cycle map, ρ_{fp} , which represents the limit cycle and satisfies $\Lambda_{cyc} \hat{\rho}_{fp} = \hat{\rho}_{fp}$ [49]. The fixed point $\hat{\rho}_{fp}$, along with the stroke propagators, fully determine the qubit state throughout the fixed cycle. The existence of a single invariant of CPTP map guarantees monotonic convergence to the fixed point [49,50]. The value of $\hat{\rho}_{fp}$ is associated with a particular state of the limit cycle, from which all other states along the cycle can be calculated by applying the propagators Λ . In turn, this allows for evaluating the thermodynamic variables, such as work, heat, and entropy.

Two important quantities for the finite-time thermodynamic analysis of these cycles are the von-Neumann and the energy entropies of the qubit

$$\mathcal{S}_{v.n} \equiv -\text{tr} [\hat{\rho} \ln \hat{\rho}] = - \left(\frac{1}{2} - \frac{\bar{S}}{\hbar} \right) \log \left(\frac{1}{2} - \frac{\bar{S}}{\hbar} \right) - \left(\frac{1}{2} + \frac{\bar{S}}{\hbar} \right) \log \left(\frac{\bar{S}}{\hbar} + \frac{1}{2} \right) , \tag{8}$$

and

$$\mathcal{S}_H = -p_H \ln p_H - (1 - p_H) \ln (1 - p_H) , \tag{9}$$

where $p_H = \left(\frac{1}{2} - \frac{\bar{S}_H}{\hbar} \right)$. Generally, we have $\mathcal{S}_H \geq \mathcal{S}_{v.n}$ with equality when the state is diagonal in the energy representation. At equilibrium, both entropies reduce to $\mathcal{S}_{v.n}(\bar{S}_{eq})$, where \bar{S}_{eq} is given

in Equation (6). The difference between the energy entropy and the von-Neumann entropy is a quantifier [51–54] of coherence. It is commonly known as the divergence [55]

$$\mathcal{D}(\hat{\rho}|\hat{\rho}_d) = \text{tr}\{\hat{\rho} \ln \hat{\rho} - \hat{\rho} \ln \hat{\rho}_d\} = \mathcal{S}_H - \mathcal{S}_{v.n} , \tag{10}$$

where $\hat{\rho}_d$ is diagonal in the energy representation and defined in Equation (13). During the cycle’s operation, the unitary strokes $\Lambda_{c \rightarrow h}$ and $\Lambda_{h \rightarrow c}$ maintain a constant von-Neumann entropy, while the energy entropy may increase with the generation of coherence.

3. Frictionless Engines

A non-vanishing heat transport rate is a prime source of irreversibility. Such heat transfer occurs when there exists a temperature gap on the interface between the engine and the baths. The influence of a realistic heat transport on cycle performance was first addressed by the classical endoreversible model [7]. Such a cycle assumes an empirical Newtonian heat transport law in order to describe the heat rate. For the qubit engine, we can replace the empirical Newtonian heat transport law with a quantum first principle derivation. The starting point is the composite Hamiltonian:

$$\hat{H}_{tot} = \hat{H}(t) + \hat{H}_{h/c} + \hat{H}_{s-h/c} , \tag{11}$$

where $\hat{H}_{h/c}$ are the hot and cold bath Hamiltonians and $\hat{H}_{s-h/c}$ represent the system-bath interaction, correspondingly. Reduced equations of motion for the system are obtained in the framework of the theory of open quantum systems [56]. This theory constitutes a general setting from which the dynamics can be derived from first principles, by employing a number of idealizations. The main assumptions, which are included in the derivation, are weak system-bath coupling and a separation of timescales between a fast bath and a sluggish system [13]. These assumptions are justified on the basis of physical reasoning and the fact that the obtained dynamical equations are indisputably consistent with the laws of thermodynamics [12,35].

To concentrate only on heat transport we can assume $\epsilon(t) = 0$, therefore $\Omega(t) = \omega(t)$, which leads to

$$\hat{H}^{elem}(t) = \hat{H}(t)_{\epsilon=0} = \Omega(t)\hat{S}_z = \omega(t)\hat{S}_z . \tag{12}$$

We refer to Equation (12) as the elementary Hamiltonian. For such a case, the Hamiltonian satisfies $[\hat{H}^{elem}(t), \hat{H}^{elem}(t')] = 0$, which decouples the dynamics of the populations and the coherence. This means that when the qubit is initialized in a diagonal state in the energy basis, the dynamics that are generated by the elementary Hamiltonian remain on the energy shell and are equivalent to frictionless solutions (cf. Section 4) of stochastic dynamics. For such instant, the analysis has common features with quantum adiabatic dynamics [57]. The state of the system then becomes:

$$\hat{\rho}_d = \frac{1}{2}\hat{I} + \frac{2}{(\hbar\Omega)^2}\langle \hat{H}^{elem} \rangle \hat{H}^{elem} , \tag{13}$$

which is diagonal in the energy representation, implying that $[\hat{\rho}_d, \hat{H}^{elem}] = 0$, $\bar{S} = -|\langle \hat{S}_z \rangle|$ and $\mathcal{S}_{v.n} = \mathcal{S}_E$. When the initial state exhibits quantum coherence, Equation (4), under these operating conditions and after a sufficient time, any initial coherence decays to zero. We will refer to this model as the elementary qubit engine.

In this framework, the reduced dissipative dynamics of the qubit is of the following structure [34]

$$\frac{d}{dt}\hat{\rho} = -\frac{i}{\hbar}[\hat{H}^{elem}(t), \hat{\rho}] + \mathcal{L}_D(\hat{\rho}) \tag{14}$$

where the dissipator \mathcal{L}_D has a Gorini–Kossakowski–Lindblad–Sudarshan form (GKLS) [10,11]

$$\mathcal{L}_D(\rho) = \frac{4}{\hbar^2} \left[k_{\uparrow}(t) \left(\hat{S}_+ \hat{\rho} \hat{S}_- - \frac{1}{2} \{ \hat{S}_- \hat{S}_+, \hat{\rho} \} \right) + k_{\downarrow}(t) \left(\hat{S}_- \hat{\rho} \hat{S}_+ - \frac{1}{2} \{ \hat{S}_+ \hat{S}_-, \hat{\rho} \} \right) \right] \tag{15}$$

where $\hat{S}_{\pm} = \hat{S}_x \pm i\hat{S}_y$ and k_{\uparrow} and k_{\downarrow} obey instantaneous detailed balance:

$$\frac{k_{\uparrow}(t)}{k_{\downarrow}(t)} = e^{-\frac{\hbar\Omega(t)}{k_B T}} . \tag{16}$$

The kinetic coefficients typically have a power dependence on Ω : $k_{\downarrow}(t) \propto \Omega(t)^n$, where $n \in \mathbb{R}$ depends on the spectral properties of the bath [56]. An alternative representation of the dynamics utilizes the Heisenberg picture, in which the equations of motion are of the form

$$\frac{d}{dt} \hat{X} = \frac{i}{\hbar} [\hat{H}^{elem}(t), \hat{X}] + \mathcal{L}_D^*(\hat{X}) + \frac{\partial}{\partial t} \hat{X} ; \tag{17}$$

where $\mathcal{L}_D^*(\bullet)$ is the adjoint generator. The relation to thermodynamics is achieved by setting $\hat{X} = \hat{H}$ and identifying the rate of change of the average energy as the quantum dynamical version of the first law of thermodynamics [58,59]

$$\frac{d}{dt} E = \mathcal{P} + \mathcal{Q} , \tag{18}$$

where: $\mathcal{P} = \langle \frac{\partial}{\partial t} \hat{H} \rangle$ is the power and $\mathcal{Q} = \langle \mathcal{L}_D^*(\hat{H}) \rangle$ is the heat flux. Power is associated with the unitary part of the dynamics, for which the von-Neumann entropy remains constant, and heat flux is identified as the average energy transfer that induces entropy change. For the elementary qubit system, the power becomes

$$\mathcal{P} = \bar{S}_H(t) \frac{\partial \omega(t)}{\partial t} \tag{19}$$

This result is analogous to the classical definition of power, where $\partial \omega / \partial t$ takes the role of the generalized force and the polarization is its conjugate variable. The expression for the heat flux reads

$$\mathcal{Q} = -\Gamma(t) \left(\langle \hat{H}^{elem}(t) \rangle - \langle \hat{H}_{eq}(\Omega(t), T) \rangle \right) , \tag{20}$$

where $\Gamma = k_{\uparrow} + k_{\downarrow}$. $\langle \hat{H}_{eq}(\Omega(t), T) \rangle = \Omega(t) \bar{S}_{eq}(\Omega(t))$ and $\bar{S}_{eq}(\Omega(t))$ is the instantaneous attractor (cf. Equation (56)), which is defined by the changing frequency $\Omega(t)$, Equation (6). As expected, the heat flux is proportional to the deviation from equilibrium and the relaxation rate. Equation (20) is identical to that one employed in [60], replacing Γ by τ_{eq}^{-1} .

The equilibration of energy is accompanied by decay of coherence. The coherence dynamics are obtained by substituting \hat{S}_x or \hat{S}_y for \hat{X} in Equation (17), leading to

$$\frac{d}{dt} \begin{bmatrix} \hat{S}_x \\ \hat{S}_y \end{bmatrix} = \begin{bmatrix} -\frac{1}{2}\Gamma(t) & -\Omega(t) \\ \Omega(t) & -\frac{1}{2}\Gamma(t) \end{bmatrix} \begin{bmatrix} \hat{S}_x \\ \hat{S}_y \end{bmatrix} . \tag{21}$$

This set of equations reflects the separation of the coherence dynamics from the population dynamics [12]. It implies that any initial coherence will decay to zero once the limit cycle is reached. This mode of operation is equivalent to stochastic thermodynamics where all thermodynamic observables are obtained in terms of the populations of the energy levels [61–63].

3.1. Elementary Cycles

Utilizing the quantum description of heat transport, introduced above, we can assemble a finite-time model of a heat engine. We construct a Carnot-type cycle and an Otto cycle whose working fluids are governed by elementary Hamiltonians, Equation (12) and then compare their finite-time

thermodynamic performance. We will compare the work produced per cycle $-\mathcal{W}$ and heat $Q_{h/c}$, which define the efficiency: $\eta = -\frac{\mathcal{W}}{Q_h}$.

3.2. Elementary Carnot-Type Cycle

Consider a quantum version of a finite-time Carnot-type cycle that is shown in Figure 3. When in contact with the heat bath, the qubit of the endoreversible engine maintains a constant internal temperature T' , generating a temperature gap with the bath. In this scenario, one can optimize the power by varying the temperature gap [64]. The efficiency then shows a monotonic decrease with the deviation from the ideal Carnot cycle: $\eta_C \geq \eta \geq 0$.

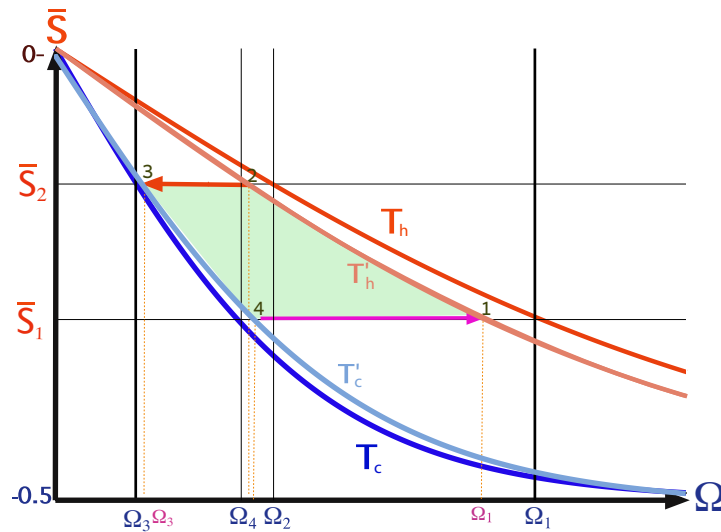


Figure 3. Endoreversible Carnot cycle: Polarization \bar{S} as a function of frequency Ω . The hot and cold isotherms are designated in red and blue, correspondingly. Blue frequencies designate the corners of the reversible Carnot cycle and the small purple frequencies correspond to the corners of the endoreversible cycle. The endoreversible frequencies depend on the cycle time; in the quasi-static limit they converge to the frequencies of the reversible Carnot cycle. The finite-time engine follows internal hot $1 \rightarrow 2$ and cold $3 \rightarrow 4$ isotherms (light red and blue curved lines) with associated temperatures T'_h and T'_c , allowing for finite heat transport. The area in green equals the total work output.

At the high temperature limit the performance is very similar to the Curzon-Ahlborn empirical model [7,65] or low dissipation limit [66], where the heat conductance was modelled by the Newtonian heat transfer law. In this limit, the efficiency at maximum power converges to

$$\eta_{CA} = 1 - \sqrt{\frac{T_c}{T_h}} \quad (22)$$

and the work per cycle becomes half the reversible work, Equation (26), $\mathcal{W}_{CA} = \frac{1}{2}\mathcal{W}_C$. The optimal power at high temperature can be approximated as [64]

$$\mathcal{P}_{Carnot}^{Endo} = \Gamma k_B \left(\sqrt{T_h} - \sqrt{T_c} \right)^2 \frac{2}{\hbar^2} \left(\bar{S}_2^2 - \bar{S}_1^2 \right) \frac{1}{\ln(\bar{S}_2/\bar{S}_1)} \quad (23)$$

This expression is reminiscent of the ideal work at the high temperature limit Equation (27), with a modified temperature gap. In this temperature regime, the optimum entropy production average rate per cycle obtains a similar form

$$\frac{\sigma_{cyc}^u}{\tau_{cyc}} = \Gamma \left(\frac{T_h - T_c}{\sqrt{T_c T_h}} \right) \frac{2}{\hbar^2} \left(\bar{S}_2^2 - \bar{S}_1^2 \right) \frac{1}{\ln(\bar{S}_2/\bar{S}_1)} \quad (24)$$

A similar structure to Equation (23) has been recently derived [67,68] based on a low dissipation limit.

The qubit Carnot-type cycle delivers finite power. In the limit of infinite cycle time, the cycle operates reversibly to obtain the Carnot efficiency

$$\eta_C = 1 - \frac{T_c}{T_h} . \tag{25}$$

The work per reversible cycle then becomes

$$\mathcal{W}_C = k_B \Delta T \Delta \mathcal{S}_{v,n} , \tag{26}$$

where $\Delta T = T_h - T_c$ is temperature gap and $\Delta \mathcal{S}_{v,n}$ is the change of the qubit’s von-Neumann entropy on the cold or hot isotherms. For the elementary cycles, the von-Neumann and energy entropy S_E coincide, as the state remains on the energy shell. Another important characteristic of the engine is the compression ratio $\mathcal{C} = \Omega_{max}/\Omega_{min}$, for the ideal Carnot engine $\mathcal{C}_{Carnot} = \Omega_1/\Omega_3$, see Figure 3. The entropy of the qubit is bounded by $\ln 2$, giving a maximum possible work of $\max(\mathcal{W}_C) = k_B(T_h - T_c)\ln(2)$.

At the high temperature limit $\hbar\Omega \ll k_B T$ the energy entropy can be approximated as $\mathcal{S}_{v,n} \simeq -\ln 2 + 2 \left(\frac{\bar{S}}{\hbar}\right)^2$ and the work becomes

$$\mathcal{W}_C \simeq k_B \Delta T \frac{2}{\hbar^2} (\bar{S}_2^2 - \bar{S}_1^2) . \tag{27}$$

This typical dependence is a general feature of any entropy dependent variable. The characteristic quadratic functionality of the polarization stems from the proximity to the maximum entropy point.

3.3. Elementary Otto Cycle

We consider an Otto cycle that is embedded within the same isotherms and frequency range of the elementary Carnot cycle and it is limited by the polarizations \bar{S}_1 and \bar{S}_2 , see Figure 4 [63]. For an engine operation mode, the compression ratio of the Otto cycle is constrained by $\mathcal{C}_{Otto} = \Omega_c/\Omega_h \leq \mathcal{C}_{Carnot}$. The engine’s work obtains the simple form

$$\mathcal{W}_{Otto} = \Delta\Omega \Delta\bar{S} , \tag{28}$$

where $\Delta\Omega = \Omega_h - \Omega_c = \Omega_2 - \Omega_4$ and $\Delta\bar{S} = \bar{S}_2 - \bar{S}_1$. It is represented geometrically by the confined area between the frequencies and polarizations, colored as light green in Figure 4. Such an engine is characterized by a constant efficiency

$$\eta_{Otto} = 1 - \frac{\Omega_c}{\Omega_h} , \tag{29}$$

which leads to $\eta_{Otto} = 1 - \frac{\bar{S}_2 T_c}{\bar{S}_1 T_h} \leq \eta_C$ for the analyzed cycle. When $\bar{S}_2 \rightarrow \bar{S}_1$, the cycle operation becomes reversible and the Carnot bound is recovered $\eta_{Otto} \rightarrow \eta_C$. This limiting case is the transition point between the engine and refrigerator operation mode ($\mathcal{C}_{Otto} = \mathcal{C}_{Carnot}$).

The heat that is dissipated during the cycle operation leads to a rise in entropy. The entropy production per cycle obtains the form

$$\sigma_{cyc}^u = \frac{1}{k_B} \left(\frac{\Omega_h}{T_h} - \frac{\Omega_c}{T_c} \right) \Delta\bar{S} . \tag{30}$$

We obtain a linear dependence on the polarization difference, which contrasts with the endoreversible result at high temperature, Equation (24), characterized by a quadratic difference dependence.

We can compare between the geometric interpretation of the work output of the elementary Otto and Carnot cycles, Equations (26) and (28). In the Otto cycle work is represented by the area that is enclosed by the cycle in the (Ω, \bar{S}) plane, and in the $(T, \mathcal{S}_{v.n})$ plane for the Carnot cycle, see description in the caption of Figure 3.

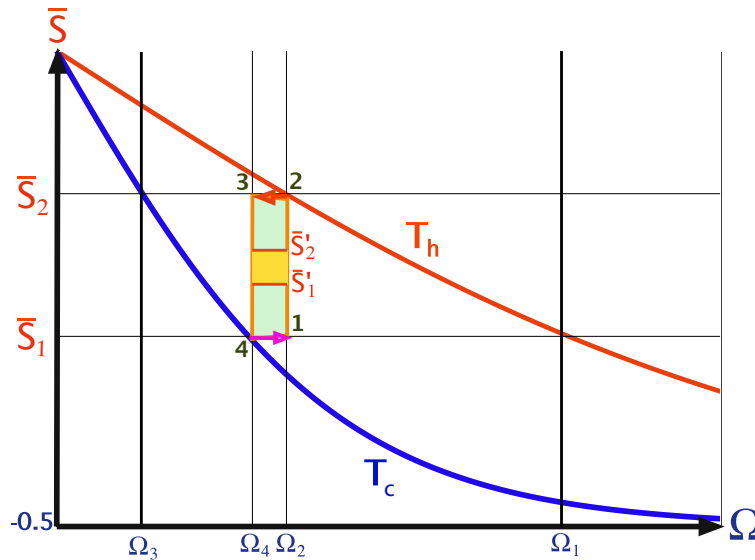


Figure 4. Otto cycle embedded within the Carnot cycle: Polarization \bar{S} as a function of frequency Ω . The same extreme polarizations \bar{S}_1 and \bar{S}_2 are used. The area in light green is the work output. The area in orange represents a finite-time Otto engine operating between \bar{S}'_2 and \bar{S}'_1 . The compression ratio C_{Otto} is reduced relative to C_{Carnot} as $\Omega_2 < \Omega_1$ and $\Omega_3 < \Omega_4$.

3.4. Optimization of the Elementary Otto Cycle

A modification of the present cycle includes optimizing the work per cycle with respect to the frequency Ω_2 . At the high temperature limit $\hbar\Omega \ll k_B T$, this optimization procedure leads to $\mathcal{W}_{max} = \frac{\hbar^2 \Omega_4^2}{k_B T_h} \left(1 - \left(\frac{T_c}{T_h}\right)^2\right)$ with efficiency $\eta_{Otto} = 1 - \frac{2T_c}{T_h + T_c}$. Such an optimization is equivalent to a maximization of the area of a rectangular region embedded within the Carnot cycle.

Finite power is obtained when the working medium does not completely relax to thermal equilibrium during the open strokes. Power optimization is carried out with respect to the thermalization time. Surprisingly, the optimal cycle was found to be of the bang-bang type, with a vanishing cycle time. The optimal power becomes [63]

$$\mathcal{P}_{Otto}^{B.B} = \frac{1}{4} \Gamma \Delta \Omega \Delta \bar{S} \tag{31}$$

where $\Gamma_h = \Gamma_c = \Gamma$. This gives a simple relation to the maximum work $\mathcal{P}_{Otto} = \frac{\Gamma}{2} \mathcal{W}_{Otto}$, Equation (28). Such an engine operates at the polarization $\bar{S} = \frac{1}{2}(\bar{S}_2 + \bar{S}_1)$. We refer to cycles with vanishing cycle times as sudden cycles. A generalization of Equation (31) for different relaxation rates Γ on the hot and cold side can be found in [69]. A sudden type qubit refrigerator Otto cycle has also been investigated with similar conclusions [70,71].

The optimal power of the endoreversible Carnot cycle Equation (23) can be compared with the Otto cycle Equation (31) at the high temperature limit. The comparison shows that the optimal power of the Otto cycle may exceed the power of an endoreversible Carnot cycle with the same polarization and bath temperatures.

The counter intuitive result where the optimum power for the Otto cycle is obtained for vanishing cycle time can be understood by noting that the largest temperature gaps between the qubit and the reservoir is at the initial portion of each open stroke. Thus, the shorter the cycle time, the faster the heat

transfer, yielding an endpoint optimum (zero cycle time) for maximum power. If we put a restriction on the minimum time allocation of the unitary strokes, then the power becomes optimal for a finite cycle time [63]. This was the original motivation for adding friction phenomenologically [72]. An important outcome of the incorporation of phenomenological friction within the model is a minimum cycle time for an engine operation. The phenomenological friction is taken to be inversely proportional to the stroke time. Thus, rapid driving leads to enhanced friction, reducing the power. Below, a minimum cycle time the output power vanishes and the cycle operates as an accelerator or a dissipator, converting useful work to heat. In a dissipator, work is consumed ($\mathcal{W} > 0$), while heat is dissipated to both the hot and cold baths ($Q_h, Q_c < 0$). Using the efficiency definition, $\eta \equiv -\mathcal{W}/Q_h$, the “efficiency” exceeds one. An accelerator operation mode includes positive work, accelerating the transfer of heat from the hot to the cold bath ($Q_h > 0$ and $Q_c < 0$). This leads to negative values of η .

4. The Quantum Origin of Friction

Quantum friction is associated with the consumption of energy in the generation of coherence, which thereafter dissipates to the bath. In a sense, coherence constitutes potential work [73], and the process of coherence generation can be viewed as a temporary storage of energy in the coherence degree(s) of freedom. When these modes decay, the associated potential work is lost. In terms of the work consumption, the dissipation of coherence is equivalent to dissipation of work and amounts to an additional cost. While such dissipation generally degrades the engines performance [51,74,75], it also speeds it up.

As in classical engines, quantum friction emerges naturally under rapid external driving. The driving generates coherence, which, in turn, leads to a higher work cost and friction, but a higher speed of operation. Generation of coherence is closely related to non-adiabatic quantum dynamics, which occurs whenever the system Hamiltonian does not self-commute at different times [$\hat{H}(t), \hat{H}(t') \neq 0$] [76].

We employ the quantum qubit model to study the influence of quantum friction on the cycle performance. This model is simple enough to allow for an explicit solution and includes the sufficient condition for observing quantum friction. That is, the qubit working medium does not self commute if $\epsilon(t)$ and $\omega(t)$, in Equation (2), are not proportionate to each other. A natural time-dependent framework to describe the dynamics of the working medium employs the set of time-dependent quantum operators

$$\begin{aligned}\hat{H} &= \omega(t)\hat{S}_z + \epsilon(t)\hat{S}_x \\ \hat{L} &= \epsilon(t)\hat{S}_z - \omega(t)\hat{S}_x \\ \hat{C} &= \Omega(t)\hat{S}_y .\end{aligned}\quad (32)$$

This operator basis set $\vec{v} = \{\hat{H}, \hat{L}, \hat{C}\}^T$, completely defines the state of the working medium (cf. Appendix A)

$$\hat{\rho} = \frac{1}{2}\hat{I} + \frac{2}{(\hbar\Omega)^2} (\langle\hat{H}\rangle\hat{H} + \langle\hat{L}\rangle\hat{L} + \langle\hat{C}\rangle\hat{C}) , \quad (33)$$

which rotates with respect to the static polarization basis set Equation (4). The advantage of such a representation is the straightforward thermodynamic interpretation, where the energy, $\mathcal{E} = \langle\hat{H}\rangle$, and coherence

$$\mathfrak{C} = \frac{1}{\hbar\Omega} \sqrt{\langle\hat{L}\rangle^2 + \langle\hat{C}\rangle^2} , \quad (34)$$

have a simple geometric interpretation in the parameter space $\{\hat{H}, \hat{L}, \hat{C}\}$. The coherence measure \mathfrak{C} can be viewed as the distance of the state from a dephased state, diagonal in the energy representation. \mathfrak{C} serves as a quantifier of coherence similar to the divergence introduced in Equation (10) [54].

The cost of generating coherence can be evaluated by recalling two invariants of the unitary dynamics: the Casimir and the Casimir companion [77]. For the $SU(2)$ algebra in the \vec{v} basis, the Casimir Companion obtains the simple form

$$\bar{X} = \frac{1}{(\hbar\Omega)^2} \left(\langle \hat{H} \rangle^2 + \langle \hat{L} \rangle^2 + \langle \hat{C} \rangle^2 \right) , \tag{35}$$

and the Casimir is obtained by replacing the squares of expectation values by the expectation values of the squares, i.e., $\langle \hat{H} \rangle^2 \rightarrow \langle \hat{H}^2 \rangle$, $\langle \hat{L} \rangle^2 \rightarrow \langle \hat{L}^2 \rangle$, and $\langle \hat{C} \rangle^2 \rightarrow \langle \hat{C}^2 \rangle$. One consequence of the invariance of \bar{X} is the conservation of the polarization amplitude along a unitary (isolated) stroke. Thus, starting from an initial equilibrium state with polarization \bar{S}_i , the Casimir companion throughout the stroke becomes $\bar{X} = \bar{S}_i$ and the initial energy is $\langle \hat{H} \rangle_i = \Omega_i \bar{S}_i$. This implies that the final energy of the unitary stroke is of the form

$$\langle \hat{H} \rangle_f = \sqrt{\left(\frac{\Omega_f}{\Omega_i} \right)^2 \langle \hat{H} \rangle_i^2 - \left(\hbar\Omega_f \mathfrak{C}_f \right)^2} \approx \frac{\Omega_f}{\Omega_i} \langle \hat{H} \rangle_i - \frac{\hbar^2 \Omega_i \Omega_f}{2 \langle \hat{H} \rangle_i} \mathfrak{C}_f^2 , \tag{36}$$

where the RHS is obtained in the limit of small coherence. This relation allows identifying the quantum adiabatic energy (first term on the RHS) corresponding to the optimal process, and an additional coherence $\mathcal{W}_{fric} \equiv |\mathcal{W} - \mathcal{W}_{ideal}| \approx \frac{\hbar^2 \Omega_i \Omega_f}{2 \langle \hat{H} \rangle_i} \mathfrak{C}_f^2$, which arises from the non-adiabatic dynamics. \mathcal{W}_{fric} equals the extra work that is required to generate coherence.

We will now demonstrate that rapid unitary strokes lead to generation of coherence. Employing Equation (2), we can obtain the Heisenberg equation of motion for the unitary strokes:

$$\frac{1}{\Omega} \frac{d}{dt} \begin{pmatrix} \hat{H}(t) \\ \hat{L}(t) \\ \hat{C}(t) \end{pmatrix} = \left(\begin{pmatrix} 0 & \mu & 0 \\ -\mu & 0 & 1 \\ 0 & -1 & 0 \end{pmatrix} + \frac{\dot{\Omega}}{\Omega^2} \hat{I} \right) \begin{pmatrix} \hat{H}(t) \\ \hat{L}(t) \\ \hat{C}(t) \end{pmatrix} , \tag{37}$$

where

$$\mu = \frac{\dot{\omega}\epsilon - \omega\dot{\epsilon}}{\Omega^3} \tag{38}$$

is the adiabatic parameter.

Finite-time processes require $\mu \neq 0$, and, in the limit $\mu \rightarrow 0$, we recover the adiabatic solutions. The exact relation between the stroke duration τ_{uni} and μ depends on the protocol. Generally, it can be expressed as

$$\mu = \frac{K}{\tau_{uni}} \tag{39}$$

where $K = \left(\frac{d\omega}{ds}\epsilon - \omega \frac{d\epsilon}{ds} \right) / \Omega^3$, with $s = t / \tau_{uni}$. For constant ϵ , K simplifies to $K = \frac{1}{\epsilon} \left(\frac{\omega_i}{\Omega_i} - \frac{\omega_f}{\Omega_f} \right)$.

For protocols that keep $\mu = \text{constant}$, Equation (37) can be integrated in order to obtain the dynamical propagator Λ_{uni} . In general, a driven system’s propagator depends explicitly on two reference times, $t_{initial}$ and t_{final} . We assume that $t_{initial} = 0$ and, therefore, index the propagator only in terms of the final time. The propagator of the unitary stroke of a product form: $\Lambda_{uni}(t) = \mathcal{U}_1(t) \mathcal{U}_2(t)$, where $\mathcal{U}_1(t)$ is a scaling by the compression ratio

$$\mathcal{U}_1(t) = \mathcal{C} \hat{I} = \frac{\Omega(t)}{\Omega(0)} \hat{I} \tag{40}$$

and $\mathcal{U}_2(t)$ represents the dynamical map of the polarization. In the $\{\hat{H}, \hat{L}, \hat{C}\}$ operator basis

$$\mathcal{U}_2(t) = \frac{1}{\kappa^2} \begin{pmatrix} 1 + \mu^2 c & \kappa \mu s & \mu(1 - c) \\ -\kappa \mu s & \kappa^2 c & \kappa s \\ \mu(1 - c) & -\kappa s & \mu^2 + c \end{pmatrix} , \tag{41}$$

where $\kappa = \sqrt{1 + \mu^2}$ and $s = \sin(\kappa\theta)$, $c = \cos(\kappa\theta)$ and $\theta(t) = \int_0^t \Omega(t') dt'$.

Accelerating the driving increases μ , which, in turn, increases the coupling of the Hamiltonian \hat{H} and coherence related operators \hat{L} and \hat{C} . Therefore, rapid driving transforms energy to coherence. The constancy of the Casimir companion Equation (35) implies that, when the final state exhibits coherence, the work extraction relative to the equivalent adiabatic procedure is degraded.

4.1. Slow Driving Regime

We can use Equation (41) to estimate the additional fraction of work during the unitary strokes due to the finite-time operation. Assuming slow driving ($\mu \ll 1$ or long stroke duration), we expand \mathcal{U}_2 up to second order in the adiabatic parameter μ in order to obtain

$$\frac{\mathcal{W}_{fric}}{\mathcal{W}} \approx \mu^2 . \tag{42}$$

This expression relates the ratio of the additional work that is consumed due to friction, Equation (36), and the total work \mathcal{W} , to the adiabatic parameter. Hence, in the slow driving regime, speeding up the stroke requires additional work. The corresponding work cost for coherence generation is in accordance with the notion of geometric thermodynamic distance and the low dissipation limit [60,78]. When the dissipation becomes significant, the power loss can exceed the gain, which imposes a minimum stroke duration for engine operation.

4.2. Sudden Limit

In the opposite driving regime, including a sudden modulation of the driving parameters, the dynamical propagator is obtained by employing the sudden approximation [57]. The propagator in the sudden limit, $\tau_{uni} \rightarrow 0$, is given by

$$\Lambda_{i \rightarrow f}^{sudd} = \frac{\Omega_f}{\Omega_i} \begin{pmatrix} \cos(\Phi) & \sin(\Phi) & 0 \\ \sin(\Phi) & -\cos(\Phi) & 0 \\ 0 & 0 & 1 \end{pmatrix} , \tag{43}$$

where $\Phi = \Phi_f - \Phi_i$ is the angle of rotation between the initial and final polarizations and $\Phi = \arccos(\omega/\Omega)$. In the sudden limit, the work becomes

$$\mathcal{W} = \langle \hat{H}(0) \rangle \left(\frac{\Omega_f}{\Omega_i} \cos(\Phi) - 1 \right) , \tag{44}$$

and the ratio between the frictional and total work is

$$\left| \frac{\mathcal{W}_{fric}}{\mathcal{W}} \right| = \frac{1 - \cos(\Phi)}{|\cos(\Phi) - (\Omega_i/\Omega_f)|} . \tag{45}$$

The frictional work dissipates during the open stroke (isotherm or isochore) that takes place after the unitary stroke. For a compression protocol ($\Omega_f > \Omega_i$), the ratio can diverge, since the work may vanish when $\cos(\Phi) = \Omega_i/\Omega_f$. In contrast, during an expansion process the ratio is bounded by $\frac{2\Omega_f}{\Omega_i + \Omega_f}$.

4.3. Shortcuts to Adiabaticity

The argument that fast dynamics on the adiabats generates coherence and leads to friction like phenomena [51,76] has a loophole. The unitary dynamics on the adiabats is in principle reversible. Because the dissipation of coherence, which seals the loss, does not take place until the thermalization stroke that follows the adiabatic stroke, protocols that null the coherence at the end of the adiabat will be frictionless.

Examining Equation (41), we find that solutions for which $\cos(\theta_f) = 1$ are frictionless. These solutions impose a quantization rule on μ :

$$\mu_l = \frac{1}{\sqrt{\left(\frac{2\pi l}{\Phi}\right)^2 - 1}} \quad , \quad l = 1, 2, \dots \tag{46}$$

where we used the identity $\theta = -\Phi/\mu$ (The identity is derived by substituting Equation (62) into the expression for μ , rearranging the equation and integrating). The relation between μ and the stroke duration leads to the minimum constant μ frictionless stroke duration

$$\tau_{uni}(l = 1) = K\sqrt{\left(\frac{2\pi}{\Phi}\right)^2 - 1} . \tag{47}$$

Adiabatic trajectories that begin and end with no coherence are frictionless (cf. Figure 5). In the limit of small and constant ϵ we get $\tau_{uni}(l = 1) \propto \epsilon(\frac{1}{\omega_f^2} - \frac{1}{\omega_i^2})$. These frictionless protocols are termed shortcuts to adiabaticity (STA) [79,80]. At intermediate times coherence is generated that requires extra work, but, if there is no dissipation in the drive, then this coherence is converted back by the working medium, arriving at the final target with no coherence. The associated speedup [79,80] may come with an accompanying cost if the control is prone to additional dissipation. Here, we consider the ideal case, assuming no dissipation and view the temporary investment of energy as a catalytic process since this energy can in principle be recouped [81]. An opposite viewpoint considers the average energy, stored during the shortcut, as wasted work [82–85].

Can the protocol duration be shortened further while keeping the frequency between its initial and final values? This is a problem in the framework of quantum control, a field which governs tasks related to manipulation of quantum systems by external fields under defined restrictions. The present control task is to transfer an initial thermal state $\hat{\rho}_i = \frac{1}{Z}e^{-\hat{H}_i/k_B T}$ to a final thermal state $\hat{\rho}_f = \frac{1}{Z}e^{-\hat{H}_f/k_B T}$ as fast as possible on the unitary strokes of the cycle. Optimal control theory has been applied to address this task [86], obtaining the minimum time solution, a so-called Fastest Effectively Adiabatic Transition (FEAT) [87]. The task of minimizing the time can be reduced to minimize $\int \hat{S}_z d\hat{S}_x$ while following the dynamics generated by Equation (2), which here gives

$$\frac{d\hat{S}_z}{d\hat{S}_x} = -\frac{\omega}{\epsilon} . \tag{48}$$

For fixed ϵ and for ω in the range $\omega_i < \omega(t) < \omega_f$, the geometric solution is to keep the curve as close to the \hat{S}_x axis as possible until the last moment to reach the final state, at which time the solution switches to the steepest curve possible [86]. Thus, the solution is of the bang-bang type, switching from the initial $\omega = \omega_i$ to the final $\omega = \omega_f$ to get the process started, keeping $\omega(t) = \omega_f$ for time $0 \leq t < \tau_1$, switching back to $\omega(t) = \omega_i$ for a time $\tau_1 \leq t < \tau_1 + \tau_2$, and finally switching to $\omega(\tau_1 + \tau_2) = \omega_f$ to reach the final state. The resulting two line segment trajectory is shown in Figure 5. The coherence that us generated during this protocol can be seen as the distance from the purple quarter-circle of zero coherence. The total FEAT time reads

$$\tau_{uni}(opt) = \tau_1 + \tau_2 = \left(\frac{1}{2\Omega_i} + \frac{1}{2\Omega_f} \right) \arccos(\zeta) \tag{49}$$

where $\zeta = \frac{\Omega_i\Omega_f(\epsilon^2 + \omega_i\omega_f) - (\epsilon^2 + \omega_i\omega_f)^2}{\epsilon^2(\omega_i - \omega_f)^2}$. While the FEAT time is much shorter than the time for a constant μ protocol, $\tau_{uni}(opt) < \tau_{uni}(l = 1)$, the FEAT solution does pay a significantly higher price in intermediate coherence.

Additional insight can be obtained by adding another control operator; a counter-diabatic term [85,88] with the control function $v(t)$ to the Hamiltonian Equation (2)

$$\hat{H}_{CA} = v(t)\hat{S}_y . \tag{50}$$

This term generates a rotation around the y axis in the z, x plane that can rotate the initial to the final Hamiltonian in a rate depending on the frequency $v(t)$. If $v(0) = v(t_f) = 0$ energy is only stored temporarily in the counter-diabatic drive, which classifies it as a catalyst.

The stroke duration τ_{uni} can be geometrically bound by the quantum speed limit [36–38,83]. The task is a rotation of the state by an angle Φ on the y axis. In the counter adiabatic case Equation (50) the angle Φ is related to the action $\int v(t)dt$, which can be related to the average stored energy \bar{E} [83]; therefore, $\tau_{uni} > \Phi\hbar/\bar{E}$ which becomes $\tau_{uni} < \Phi/\bar{v}$. In other STA protocols where the Hamiltonian does not contain \hat{S}_y , the control action of rotation is obtained by the commutator $[\hat{S}_z, \hat{S}_x]$, which generates coherence. A bound can be obtained from (49), $\tau_{uni} > \Phi\hbar/\Delta E = \Phi/\Omega_{min}$, where $\hbar\Omega_{min}$ is the minimum energy gap.

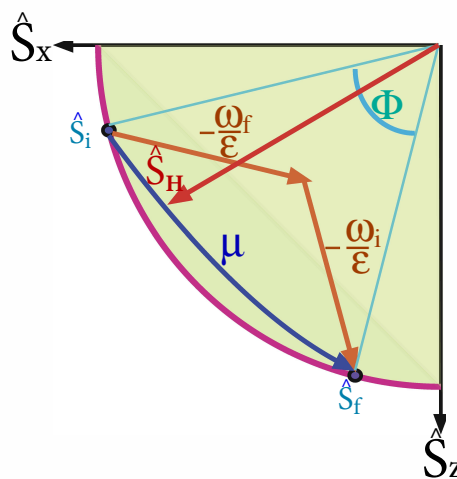


Figure 5. Optimal frictionless trajectories for the unitary stroke displayed on the polarization axis of $\langle \hat{S}_x \rangle$ and $\langle \hat{S}_z \rangle$. The radius of the semicircle is equivalent to the initial polarization $\bar{S}_i = \bar{S}_{H_i}$, which is on the energy axis. Because the unitary dynamics preserves the polarization and the chosen energy direction is on the x, z plane, the semicircle shows all the possible states on the energy axis. Any interior point possesses coherence. In orange is the optimal bang-bang protocol that is composed of two segments the first with a slope of $-\omega_f/\epsilon$ and the second $-\omega_i/\epsilon$. The blue arrow represents the constant μ protocol.

To summarize, fast frictionless protocols for the unitary strokes are possible provided the coherence is not transferred to the thermalization strokes. The price for acceleration of the stroke is the generation of intermediate coherence that requires a temporary investment of power. If no restrictions are imposed on the power invested, or analogously on the range of $\omega(t)$, the time period τ_{uni} can be shrunk to zero. Another scheme to achieve a vanishing time period includes adding an unrestricted counter-diabatic term, Equation (50), to the Hamiltonian [85]. For a more realistic description of the storage device, restriction on the control are introduced. One possible restriction is to limit the averaged stored energy. Another possibility is to restrict coherence. In principle, all of the temporary power can be retrieved in the external controller when the drive is completely isolated. However, in practice, this is an idealization, and any real storage device is sure to have some dissipation. Thus, one expects some dissipation from the controller [89].

5. Thermalization

Thermalization is the process of relaxing the system toward equilibrium with an external heat reservoir, e.g., the hot or cold baths. The relaxation is mediated by the system-bath interaction term $\hat{H}_{s-h/c}$ (Equation (11)), which generally depends on both the system and bath operators, as well as the coupling strength g . The question arises, can we actively influence the thermalization process? Three options for control are possible. The first, which we consider here, is to control the system Hamiltonian [90,91], the second is to vary the coupling strength [92,93], and the third is controlling the temperature of the bath.

5.1. Isochoric Thermalization

When compared to quantum Carnot-type cycles the analysis of the quantum Otto cycle is simplified, since the thermalization strokes are carried out at constant frequency Ω . For this reason, it has been thoroughly studied, and originally constituted the main platform to investigate thermodynamics at the quantum level [94,95].

By definition, during an isochore the Hamiltonian is static. Consequently, the only adjustable control parameter of the thermalization is the contact time with the bath. This is equivalent to adjusting the system bath coupling. The dynamics along the stroke is described by Equations (14) and (15) with a constant Hamiltonian. These lead to transfer of energy and exponential decay of coherence, Equation (21), until the system reaches equilibrium.

5.2. Isothermal Thermalization

Here, we concentrate on the finite-time thermalization strokes, which transfer heat to and from the engine. Within the limits that are imposed by the isotherms of the working medium, we can find various choices for cycles with finite power [96–98].

Thermalization can be controlled by the varying Hamiltonian, while the system is simultaneously coupled to the bath. We now consider the general case, where the Hamiltonian does not commute with itself at different times, $[\hat{H}(t), \hat{H}(t')] \neq 0$. A prerequisite for obtaining control is to derive a dynamical description that is accurate and consistent with thermodynamics. Such a dynamical description has been formulated in Ref. [34], where a Non-Adiabatic Master Equation (NAME) was developed that incorporated the effect of the external driving.

Within this framework, we can address the issue of actively speeding up the thermalization. Typically, the rate of approaching equilibrium is proportional to deviation of the state from the fixed point of equilibrium. As we get closer to the target, the rate decreases. Broadly speaking, the strategy of speeding up the thermalization is to first generate coherence that moves the system away from the instantaneous attractor. Consequently, the relaxation is enhanced. At the final stage the system is rotated, converting the coherence to energy to reach the desired thermal state. The speedup comes with a price since, in contrast to the unitary strokes, during the open strokes we cannot separate the unitary drive from the dissipative loss.

5.3. Shortcut to Equilibrium Protocols

Shortcut to equilibrium protocols (STE) are active control protocols, generating a rapid transition between two equilibrium states with different Hamiltonians, while the system is coupled to a bath of a fixed temperature. This control task requires modifying the system entropy, in contrast to the common scheme of unitary control. The shortcut protocols fall within the framework of control of open quantum systems. The rules of the game that we consider restrict the active control to only the system Hamiltonian. The bath Hamiltonian is set and cannot be controlled, and the bath remains in a thermal state due to its enormous size and negligible influence of the qubit.

In the presence of non-adiabatic driving, the external field dresses the system, which consequently effectively modifies the system-bath interaction. As a result, the external driving enables indirect

coherent control of the system's dissipative dynamics. As previously stated, the control of the qubit state during the isothermal strokes requires prior knowledge of the open system dynamics. In turn, to describe the reduced dynamics of the open system, one first requires a closed form solution of the driven isolated system. To be specific, the derivation of the Non-Adiabatic Master Equation (NAME) requires, as an input, the free dynamics of the driven system [34]. The solution is non-trivial in the presence of non-adiabatic driving, when the Hamiltonian does not commute with itself at different times. For arbitrary driving, constructing an explicit solution of the dynamical propagator requires a time-ordering procedure [57].

We have developed an algebraic procedure in order to circumvent the time-ordering problem by employing a dynamical operator basis. This technique is closely related to the inertial theorem [99]. The theorem implies that, for a closed operator algebra, the dynamical propagator can be obtained for a family of non-adiabatic protocols, characterized by a slow 'acceleration' of the drive. The associated solutions and driving protocols are termed inertial solutions and protocols. These solutions are conveniently expressed as linear combinations of the eigenoperators of the propagator.

For the qubit working medium, as represented by Equation (2), the inertial protocol is characterized by a slowly varying adiabatic parameter, i.e., $\frac{1}{\Omega} \frac{d\mu}{dt} \ll 1$. Under this condition, the dynamics approximately follows the inertial solution. This solution is conveniently expressed in terms of the dynamics of the basis of operators $\vec{v}(t) = \{\hat{H}, \hat{L}, \hat{C}\}^T$ Equation (32)

$$\vec{v}(t) = \frac{\Omega(t)}{\Omega(0)} P(\mu(t)) e^{-i \int_0^t D(t') \Omega(t') dt'} P^{-1}(\mu(t)) \vec{v}(0) , \quad (51)$$

where P is a 3 by 3 matrix that is dependent on the instantaneous adiabatic parameter $\mu(t)$, see Appendix B, and $D = \text{diag}(0, \kappa, -\kappa)$ with $\kappa = \sqrt{1 + \mu^2}$. The three operators obtained from $(\hbar\Omega(t))^{-1} P^{-1} \vec{v}(t)$ are eigenoperators of the propagator. We introduce a scaled version of these operators $\vec{g} = \{\hat{\chi}, \hat{\sigma}, \hat{\sigma}^\dagger\}^T$, satisfying an eigenvalue type relation $\hat{\sigma}^H(t) = \hat{U}^\dagger(t) \hat{\sigma}(0) \hat{U}(t) = e^{-i \int_0^t dt' \kappa(t') \Omega(t')} \hat{\sigma}(0)$, where $\hat{U}(t)$ is the propagator and superscript H designates operators in the Heisenberg picture. The operator $\hat{\chi}^H(t) = \hat{\chi}(0)$ is the inertial invariant, i.e., the eigenoperator with a vanishing eigenvalue. Expressing the eigenoperators in terms of the $\{\hat{H}, \hat{L}, \hat{C}\}$ basis, we obtain

$$\begin{aligned} \hat{\chi}(t) &= \frac{\sqrt{2}}{\kappa \hbar \Omega} (\hat{H} + \mu \hat{C}) \\ \hat{\sigma}(t) &= \frac{1}{\kappa \hbar \Omega} (-\mu \hat{H} - i\kappa \hat{L} + \hat{C}) , \end{aligned} \quad (52)$$

where all of the parameters may be time-dependent. The eigenoperators in \vec{g} are orthonormal with respect to the inner product in Liouville space, $(\hat{A}, \hat{B}) = \text{tr}\{\hat{A}^\dagger \hat{B}\}$, and satisfy the $SU(2)$ commutation relations of the form $[\hat{\sigma}, \hat{\sigma}^\dagger] = -\sqrt{2} \hat{\chi}$, $[\hat{\chi}, \hat{\sigma}] = -\sqrt{2} \hat{\sigma}$. Appendix A summarizes the relation between the various basis sets of expansion operators $\vec{s} = \{\hat{S}_x, \hat{S}_y, \hat{S}_z\}^T$, $\vec{v} = \{\hat{H}, \hat{L}, \hat{C}\}^T$ and $\vec{g} = \{\hat{\chi}, \hat{\sigma}, \hat{\sigma}^\dagger\}$, see also Figure 1 for a geometric representation.

Combining the inertial solution, Equation (51), for the isolated system dynamics with the NAME leads to a master equation for a broad range of driving protocols. The master equation is valid from the first principles under the following conditions: (i) the bath dynamics are rapid relative to the typical timescales of both the system and the driving, τ_s and τ_d , i.e., $\tau_b \ll \tau_s, \tau_d$, where τ_b is the typical timescale of the decay of correlations in the bath; (ii) the system-bath relaxation time τ_r is large relative to the system and bath timescales, i.e., $\tau_r \gg \tau_s, \tau_b$; and, (iii) the driving protocol satisfies the inertial condition, $\frac{1}{\Omega} \frac{d\mu}{dt} \ll 1$. Condition (i) is associated with Markovian dynamics and (ii) corresponds to a weak system-bath interaction, which is also known as the weak coupling limit [13,56].

In the interaction picture relative to the system-bath bare Hamiltonian, the qubit’s open system dynamics obtains the familiar GKLS form [91]

$$\frac{d}{dt}\tilde{\rho} = \tilde{\mathcal{L}}(t)[\tilde{\rho}] = k_{\downarrow}(\alpha(t))\left(\hat{\sigma}\tilde{\rho}(t)\hat{\sigma}^{\dagger} - \frac{1}{2}\{\hat{\sigma}^{\dagger}\hat{\sigma},\tilde{\rho}(t)\}\right) + k_{\uparrow}(\alpha(t))\left(\hat{\sigma}^{\dagger}\tilde{\rho}(t)\hat{\sigma} - \frac{1}{2}\{\hat{\sigma}\hat{\sigma}^{\dagger},\tilde{\rho}(t)\}\right). \tag{53}$$

Here, $\hat{\sigma}$ and $\hat{\sigma}^{\dagger}$ designate operators at initial time and overscript tilde denotes operators in the interaction picture. The kinetic coefficients of Equation (53) depend on the spectral features of the bath and the effective time-dependent frequency α . This frequency serves as an effective generalized Rabi frequency of the driven system

$$\alpha(t) = \kappa(t)\Omega(t) = \sqrt{1 + \mu(t)^2}\Omega(t). \tag{54}$$

In the quantum adiabatic regime, $\mu \rightarrow 0$ and α converges to the instantaneous Rabi frequency, $\Omega(t)$. For $\mu > 0$, the effective frequency $\alpha(t) > \Omega(t)$. This is the outcome of an effective dressing of the system by the driving. As a consequence of the rapid driving, the bath interacts with the dressed system, which leads to deviations from the adiabatic dynamics. For the general case, there may be multiple effective frequencies $\{\alpha\}$. Their exact form depends on a particular system-bath interaction and the defined spectral density [34,91].

For the present analysis, we assume a bosonic bath with an Ohmic spectral density. The system-bath interaction is taken as $\hat{H}_{sb} = ig\sum_k\sqrt{\frac{2\pi\omega_k}{V\hbar}}(\hat{b}_k - \hat{b}_k^{\dagger})\hat{S}_y$, where \hat{b}_k^{\dagger} and \hat{b}_k are the creation and annihilation operators of the k ’th bath oscillator, and ω_k is the oscillator frequency. The coupling strength is represented by g and V is the reservoir size. For a large reservoir in equilibrium, the kinetic coefficients become

$$k_{\downarrow}(\alpha) = \frac{g^2\alpha}{\hbar c\kappa}(1 + N(\alpha)) \tag{55}$$

$$k_{\uparrow}(\alpha) = \frac{g^2\alpha}{\hbar c\kappa}N(\alpha).$$

where c is the speed of event propagation in the bath and $N(\alpha) = 1/(\exp(\hbar\alpha/k_B T) - 1)$ is the Bose–Einstein distribution, characterizing the correlations between bath modes at frequency α . It is simple to verify that these kinetic coefficients satisfy detailed balance with respect to α , Equation (16). This property is essential for a thermodynamically consistent dynamical description [12,35]. In the adiabatic limit, the kinetic coefficients converge to adiabatic rates and the Lindblad jump operators to the creation annihilation operators of the two-level system. As expected, Equation (53) then converges to the adiabatic master equation [33].

The NAME of the driven qubit, Equation (53) propagates the qubit state in the direction of the instantaneous attractor. The attractor is defined by the relation

$$\mathcal{L}(t)[\tilde{\rho}_{i,a}] = \tilde{\rho}_{i,a}, \tag{56}$$

where $\tilde{\mathcal{L}}(t)$ is a superoperator that generates the dynamics in the interaction picture. For the qubit, the attractor is in the direction of $\hat{\chi}$, mixing energy, and coherence. The attractor is rotated by the angle $\xi = \arccos(1/\sqrt{1 + \mu^2})$ from the energy axis. The attractor can be expressed in the Gibbs form:

$$\tilde{\rho}_{i,a}(t) = Z^{-1}e^{-\frac{\hbar\alpha\hat{\chi}}{\sqrt{2}k_B T}}, \tag{57}$$

where $Z = \text{tr}\left(e^{-\hbar\alpha\hat{\chi}/\sqrt{2}k_B T}\right)$ is the partition function. In the presence of driving, the attractor varies in time, and the system continuously aspires towards a changing target, but it does not manage to reach it. Only at the initial and final times, is the driving stationary and the qubit reaches the attractor. Remember that this analysis applies for the case when $[\hat{H}(t), \hat{H}(t')] \neq 0$. When the

Hamiltonian commutes with itself at different times, as in the elementary Hamiltonian Equation (12), the instantaneous attractor becomes a Gibbs state with the instantaneous Hamiltonian $\hat{H}(t)$ and temperature T . In the adiabatic limit, when $\mu \rightarrow 0$ Equations (52), (54) and (57) lead to the same result.

The qubit control is based on the master equation, Equation (53). Our present control target is to speed up the thermalization while changing the qubit Hamiltonian. This step will be employed in the open strokes of Carnot-type engines in Section 6. Specifically, we desire a control protocol that transfers an initial Gibbs state, defined by $\Omega(0) = \Omega_i$ and temperature T , to a final Gibbs state of the same temperature and final frequency $\Omega(t_f) = \Omega_f$. Moreover, we assume that the system at the initial and final times is stationary with no external driving. The control agents are the parameters of the free Hamiltonian $\omega(t)$ and $\varepsilon(t)$. Notice that these parameters only indirectly effect the master equation. To find a control, we opt to employ a reverse engineering approach, in which we propose a trajectory for the qubit state that forms a solution to the master equation. In turn, this solution determines the kinetic coefficients of the master equation, from which we can extract the direct control parameters.

Performing the analysis in the interaction representation relative to the bare system Hamiltonian simplifies the control scheme. In this frame, the Lindblad jump operators, $\hat{\sigma}$ and $\hat{\sigma}^\dagger$, vary slowly with μ .

The control trajectory, which is a dynamical solution of Equation (53), is obtained by representing the state $\tilde{\rho}$ in terms of the basis of eigenoperators \vec{g} of the free dynamics, Appendix A:

$$\tilde{\rho} = \frac{1}{2} \hat{I} + c_\sigma \hat{\sigma} + c_{\sigma^\dagger} \hat{\sigma}^\dagger + c_\chi \hat{\chi} \quad (58)$$

where $c_r = \text{tr}(\tilde{\rho} \hat{r})$, with $r = \sigma, \sigma^\dagger, \chi$, are time-dependent coefficients. Substituting Equation (58) into (53) and utilizing the orthogonality of the eigenoperators leads to an equivalent representation of the dynamics

$$\frac{d}{dt} c_\chi = - (k_\downarrow(t) + k_\uparrow(t)) c_\chi - \frac{1}{\sqrt{2}} (k_\downarrow(t) - k_\uparrow(t)) \quad (59)$$

$$\frac{d}{dt} c_\sigma = -\frac{1}{2} (k_\downarrow(t) + k_\uparrow(t)) c_\sigma \quad (60)$$

and similarly for c_{σ^\dagger} . These equations completely determine the system dynamics and form the template for coherent control. What is missing are the boundary conditions. The choice of the initial and final Gibbs state along with the condition of stationarity at initial and final times imposes boundary conditions on Equation (60).

We can simplify the problem by eliminating Equation (60). For the boundary conditions (and any initial diagonal state in the energy representation), the coefficients $c_\sigma(0) = c_{\sigma^\dagger}(0) = 0$ and $\mu = 0$. These relations, together with Equation (60), imply that c_σ and c_{σ^\dagger} vanish at all times.

We can now focus on a single equation, Equation (59), with boundary conditions: $c_\chi(0) = -\frac{1}{\sqrt{2}} \tanh\left(\frac{\hbar\Omega(0)}{2k_B T}\right)$, $c_\chi(t_f) = -\frac{1}{\sqrt{2}} \tanh\left(\frac{\hbar\Omega(t_f)}{2k_B T}\right)$, and $\mu(0) = \mu(t_f) = 0$. In addition, the initial and final states and Equation (59) imply that $\dot{c}_\chi(0) = \dot{c}_\chi(t_f) = 0$.

To proceed, we determine the trajectory solution through the coefficient c_χ . We choose the most simple polynomial solution that is compatible with the boundary conditions. In this case, a third order polynomial is sufficient. In terms of a dimensionless parameter $s = t/t_f$, the solution reads

$$c_\chi(s) = c_\chi(0) + 3\Delta s^2 - 2\Delta s^3 \quad (61)$$

where $\Delta = c_\chi(t_f) - c_\chi(0)$. Next, we substitute the solution Equation (61) into Equation (59) and obtain the kinetic coefficients, from which we can extract $\alpha(t)$, Equation (55). These steps are achieved while utilizing a common numerical solver.

The control function $\Omega(t)$ is now evaluated by solving the master equation $\Omega = \alpha/\kappa$ for a set of defined controlled parameters $\omega(t)$ and $\varepsilon(t)$. In practice, the master equation depends on the

generalized Rabi frequency $\Omega(t)$ and $\dot{\phi}$ (through μ); this means that we have an additional freedom in the control parameters of the Hamiltonian.

We chose to parameterize the control parameters in terms of the time-dependent frequency Ω and the phase ϕ :

$$\begin{aligned}\omega(t) &= \Omega \cos(\phi) \\ \epsilon(t) &= \Omega \sin(\phi) .\end{aligned}\quad (62)$$

In this parametrization, the adiabatic parameter becomes $\mu = -\dot{\phi}/\Omega$ and the effective frequency can then be expressed as

$$\alpha = \sqrt{1 + (\dot{\phi}/\Omega)^2} \Omega . \quad (63)$$

To set the angle ϕ , we study two protocols that differ by their boundary conditions. The first is a quadratic function of time $\phi(t) = a(t - 2t^2/3t_f)$, where a is a dimensionless free parameter taken to be equal to the numerical value of $1/t_f^2$ in the model units. This protocol leads to a final value for the angle that scales with the duration time $\phi(t_f) \propto t_f$. The second protocol starts at $\phi(0) = 0$ and ends at $\phi(t_f) = \pi/2$, where the direction of the final Hamiltonian is rotated by ninety degrees relative to the initial Hamiltonian. Introducing a polynomial that complies with the boundary conditions leads to $\phi(t) = \pi t^2(3t_f - 2t)/(6t_f^3)$. Both of the protocols satisfy the required condition of stationarity at initial and final times: $\dot{\phi}(0) = \dot{\phi}(t_f) = 0$. Finally, solving Equation (63) for $\Omega(t)$ leads to the control protocol.

Overall, the constructed shortcut to equilibration (STE) protocol rapidly modifies the system entropy, transferring an initial thermal state with a Rabi frequency Ω_i to a thermal state of a frequency Ω_f at the same temperature. In Ref. [91], a different STE protocol has been introduced, utilizing a product state consisting of exponentials, see Appendix A. In contrast, here we choose a linear combination of eigenoperators, Equation (58), which is the natural approach for a system that is described by a compact algebra. This choice has the advantage of leading to a simpler analysis.

5.4. Thermodynamic Cost of Finite-Time Thermalization

Fast driving moves the system away from equilibrium, leading to enhanced dissipation. The thermodynamic cost can be characterized by the entropy production rate

$$\Sigma^u \equiv -\frac{d}{dt} \mathcal{D}(\hat{\rho}|\hat{\rho}_{i,a}) = -k_B \text{tr}(\tilde{\mathcal{L}}[\hat{\rho}] \ln \hat{\rho}) + k_B \text{tr}(\tilde{\mathcal{L}}[\hat{\rho}] \ln \hat{\rho}_{i,a}) = -k_B \text{tr}\left(\tilde{\mathcal{L}}[\hat{\rho}] \left(\ln \hat{\rho} + \frac{\hbar \alpha}{\sqrt{2}T} \hat{\chi}\right)\right) . \quad (64)$$

In the infinitely long time limit, the state $\hat{\rho}$ converges to $\hat{\rho}_{i,a}$ and the entropy production rate vanishes. The entropy production in this limit has been studied recently [100] and is related to fluctuation theorems.

During the shortcut to equilibrium protocols $c_{\sigma,\sigma^\dagger} = 0$ and the state is completely characterized by the expectation value $c_\chi = \text{tr}(\hat{\chi}\hat{\rho})$, $\hat{\rho} = \frac{1}{2}I + c_\chi \hat{\chi}$. Alternatively, this state can be represented in a Gibbs form $\hat{\rho} = Z^{-1}e^{-\beta \hat{\chi}}$. The role of β motivates introducing an effective temperature of the qubit in the interaction representation: $T' \equiv \hbar \alpha / \sqrt{2}k_B \beta$. Such a form allows for a straightforward interpretation of Equation (64); this is achieved by the following derivation. We begin by utilizing the Gibbs form of $\hat{\rho}$ and insert Equation (57) into (64) to obtain

$$\Sigma_\chi^u = k_B \left(\frac{1}{T'} - \frac{1}{T}\right) \left(\frac{\hbar \alpha}{\sqrt{2}k_B}\right) \text{tr}(\dot{\hat{\rho}} \hat{\chi}) . \quad (65)$$

This relation can be interpreted as the product of a thermodynamic force $\propto -\nabla\frac{1}{T}$ and heat current in units of the energy quanta $\hbar\alpha$. Next, we express $\dot{\rho}$ in terms of β in order to obtain: $\dot{\rho} = -(\langle\chi\rangle + 1)\dot{\beta}\dot{\rho}$, with $\langle\hat{\chi}\rangle = -\frac{1}{\sqrt{2}}\tanh\left(\frac{\beta}{\sqrt{2}}\right)$, and

$$\dot{\beta} = \text{tr}\left(\frac{d\dot{\rho}}{dt}\dot{\rho}^{-1}\hat{\chi}\right) = -\frac{1}{\sqrt{2}}\left[\left(1 + e^{-\sqrt{2}\beta}\right)k_{\downarrow} - \left(1 + e^{\sqrt{2}\beta}\right)k_{\uparrow}\right]. \tag{66}$$

Substituting Equations (55), (66) into Equation (65) leads to the final expression

$$\Sigma_{\chi}^u = \left(\frac{1}{T'} - \frac{1}{T}\right)(\hbar\alpha)\frac{k_{\downarrow}(\alpha)\langle\hat{\chi}\rangle(\langle\hat{\chi}\rangle + 1)}{2(1 + e^{\hbar\alpha/k_B T'})}\left(e^{-\hbar\alpha/k_B T'} - e^{-\hbar\alpha/k_B T}\right). \tag{67}$$

As expected, we obtain a positive entropy production. The first and last terms in the brackets have opposite signs while the expectation value of $\hat{\chi}$ satisfies $-1 < \langle\chi\rangle < 0$ for a positive temperature. This leads to a symmetric dependence on the temperature gap $\Delta T = T - T'$, i.e., the entropy production only depends on the magnitude of the gap and it is independent of whether the working medium effective temperature is hotter or colder relative to the bath temperature.

In the high temperature limit $\hbar\alpha/k_B \ll T, T'$, the relation can be further simplified, leading to entropy generation that scales as the square difference between inverse temperatures

$$\Sigma_{\chi}^u \approx -k_B k_{\downarrow} \langle\chi\rangle \left(\frac{\hbar\alpha}{2k_B}\right)^2 \left(\frac{1}{T'} - \frac{1}{T}\right)^2. \tag{68}$$

We next derive the entropy production rate for a general initial state that includes coherence, following the inertial solution, Equation (60). We begin by expressing the qubit state as a maximum entropy state $\dot{\rho} = \bar{Z}^{-1} \exp(-(\beta\hat{\chi} + \gamma_x\hat{\sigma}_x + \gamma_y\hat{\sigma}_y))$, where $\sigma_x = \frac{1}{\sqrt{2}}(\sigma + \sigma^\dagger)$ and $\sigma_y = \frac{i}{\sqrt{2}}(\sigma - \sigma^\dagger)$ see Appendix A for further details. The existence of such a form is guaranteed from the closure property of the operator algebra and the Baker–Campbell–Hausdorff formula [101]. Defining the effective thermodynamic forces \mathcal{F}_l and effective “temperature”: $\mathcal{F}_{\chi} = \frac{1}{T_{\chi}} - \frac{1}{T}$, where $T_{\chi} = \frac{\hbar\alpha}{\sqrt{2}k_B\beta}$, $\mathcal{F}_{\sigma_x} = \frac{k_B\gamma_x}{\hbar\alpha}$ and $\mathcal{F}_{\sigma_y} = \frac{k_B\gamma_y}{\hbar\alpha}$ leads to the entropy production rate:

$$\Sigma^u = \sum_{l=\chi,\sigma_x,\sigma_y} \mathcal{F}_l \mathcal{J}_l, \tag{69}$$

where $\mathcal{J}_l = \frac{\hbar\alpha}{\sqrt{2}}\text{tr}\left(\dot{\rho}\hat{l}\right)$. We can further simplify the fluxes \mathcal{J}_l by utilizing the linearity of the trace and the derivative operations and the dynamics of eigenoperators expectation values, as in Equation (60). This leads to

$$\mathcal{J}_{\chi} = -\frac{\hbar\alpha\Gamma}{\sqrt{2}}(\langle\hat{\chi}\rangle - \langle\hat{\chi}\rangle_{i.a}) ; \mathcal{J}_{\sigma_x} = -\frac{\hbar\alpha\Gamma}{2}\langle\hat{\sigma}_x\rangle ; \mathcal{J}_{\sigma_y} = -\frac{\hbar\alpha\Gamma}{2}\langle\hat{\sigma}_y\rangle, \tag{70}$$

with $\Gamma = k_{\downarrow} + k_{\uparrow}$ and $\langle\hat{\chi}\rangle_{i.a} = -\frac{1}{\sqrt{2}}\tanh\left(\frac{\hbar\alpha}{2k_B T}\right)$. The form of the entropy production rate resembles the heat transfer entropy production law of classical non-equilibrium thermodynamics [102–104], but with a nonlinear relation between flux and force. The difference between the effective inverse temperature and bath temperature constitutes the thermodynamic forces, while \mathcal{J}_l are the associated thermodynamic fluxes. The expression obtain a similar form, however, a fundamental difference between Equation (69) and the classical expression exists. In the classical expression the relations between the thermodynamic fluxes and forces is strictly phenomenological. Commonly, only the first order is considered and the fluxes are taken to be linear functions of the forces. For example, Fick’s law for diffusion of matter relates the diffusion flux to the gradient in concentration, or Fourier’s law for heat conduction relates the heat transport to the gradient of inverse temperature. In contrast,

the framework of open quantum systems, which we currently employ, allows for deriving the relation between thermodynamic fluxes and forces from a microscopic description.

In the high temperature limit when $\bar{\beta}$ and $\bar{\gamma}$ are small, we recover the linear response relation between fluxes and forces: $\mathcal{J}_\chi \approx L\mathcal{F}_\chi$, $\mathcal{J}_{\sigma_x} \approx L\mathcal{F}_{\sigma_x}$ and $\mathcal{J}_{\sigma_y} \approx L\mathcal{F}_{\sigma_y}$, where $L = \frac{\Gamma}{k_B} \left(\frac{\hbar\alpha}{2}\right)^2$, see Appendix A for further details. As a result, the entropy production rate in the linear response region becomes

$$\Sigma^u = \sum_l L\mathcal{F}_l^2 \quad (71)$$

It should be noted that the diagonal Onsager matrix is a consequence of the fact that, in the interaction representation, the dynamics of the coherence are separated from χ . Once we rotate to the $\{\hat{H}, \hat{L}, \hat{C}\}$ basis we will get symmetric coupling elements between energy and coherence in the Onsager matrix. We stress that the current derivation, leading to the linear response result, is not based on the adiabatic assumption of a perturbation with respect to the Gibbs state [78].

Overall, in the general case, we observe three independent forces and fluxes that are responsible for entropy production, a heat flux, and two fluxes that are associated with loss of coherence.

6. Local Cycles

Closing the cycles requires concatenating the four strokes. We distinguish two families of cycles that differ by the coherence operation: global or local. In local cycles, the coherence vanishes on the four switching points between strokes. Global cycles, on the other hand, maintain coherence throughout the cycle and it will be treated in Section 7.

6.1. Local Otto Cycle

Local cycles are obtained by employing shortcuts to adiabaticity (STA) on the adiabats [105,106]. The chosen protocols are characterized by a minimum unitary stroke time $\tau_{uni}(l = 1)$, which forces a finite optimum thermalization time. As a result, maximum power is obtained for a total finite cycle period [72], Figure 6 displays such a cycle.

Optimizing the thermalization period has been addressed in Ref. [63]. The main variable influencing the power output is the polarization difference $\bar{S}'_2 - \bar{S}'_1$ (cf. Figure 4). Therefore, the gaps $|S_2 - S'_2|$ and $|S_1 - S'_1|$ are optimized in order to achieve finite heat transport. The described procedure leads to [63]

$$\bar{S}'_2 - \bar{S}'_1 = (\bar{S}_2 - \bar{S}_1)F(x, y) \quad (72)$$

where $F(x, y) = \frac{(1-x)(1-y)}{1-xy}$, with $x = e^{-\Gamma_h\tau_h}$ and $y = e^{-\Gamma_c\tau_c}$. Here, τ_h and τ_c are the time allocation for thermalization. In addition, optimizing for $\Gamma_c = \Gamma_h$ leads to $\tau_h = \tau_c$. Optimizing for power under the constraint of a finite-time allocation during the unitary strokes, τ_{uni} , leads to [107]:

$$x + \Gamma\tau_{uni} = \sinh(x) \quad (73)$$

For small x , Equation (73) can be solved to obtain $\tau_h = \tau_c = \frac{1}{\Gamma}(\Gamma\tau_{uni}/3)^{1/3}$. In this limit, the optimal power of local Otto becomes

$$\mathcal{P}_{Otto}^{L.O} = \frac{1}{(\Gamma\tau_{uni}/3)^{1/3}} \frac{1}{4} \Gamma \Delta \Omega \Delta \bar{S} = \frac{1}{(\Gamma\tau_{uni}/3)^{1/3}} \mathcal{P}_{Otto}^{B.B} \quad (74)$$

which is smaller than the bang-bang power $\mathcal{P}_{Otto}^{B.B}$ Equation (31).

The power of the local Otto cycle as a function of cycle time is shown in Figure 10 displaying the typical maximum power. The efficiency of the engine $\eta_{Otto}^{L.O}$ Equation (29) is independent of cycle period (cf. Figure 9). In practice, such a cycle can be analyzed by means of stochastic thermodynamics [61], since coherence has been eliminated from the analysis by employing shortcut protocols. A similar result employing a different derivation can be found in [68].

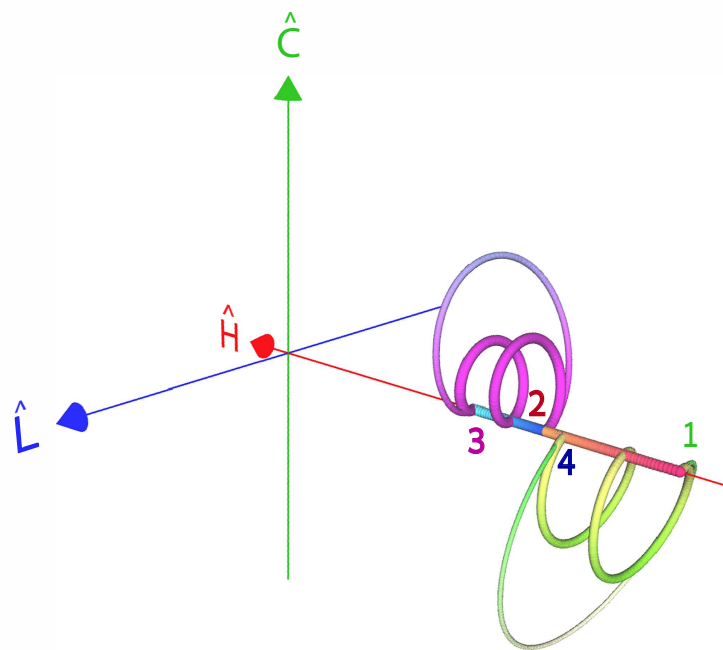


Figure 6. Frictionless shortcut (local) Otto cycle plotted in the $\{\langle\hat{H}\rangle, \langle\hat{L}\rangle, \langle\hat{C}\rangle\}$ space. The hot isochore $1 \rightarrow 2$ is represented by red thick line, and the cold isochore $3 \rightarrow 4$ is shown in blue. The expansion $2 \rightarrow 3$ and compression $4 \rightarrow 1$ unitary strokes begin and end on the energy axis, as the qubit exhibits no coherence between consecutive strokes. The fastest two solutions of shortcuts with constant μ are shown. The single large loop (thick line) corresponds to the fastest solution with $l = 1$ in Equation (46), which corresponds to τ_{min} and the second solution includes two small loops, $l = 2$.

6.2. Local Carnot Cycle

A local Carnot cycle, also called the ‘Shortcut Carnot’ cycle, is constructed by combining two shortcut to equilibrium protocols (open-strokes) and two shortcuts to adiabaticity protocols (unitary strokes), see Figure 7. It is characterized by the same cycle parameters as the Carnot cycle, while operating at finite speed, thus producing power. The increase in power does not come for free, as rapid driving increases dissipation, leading to a reduction in efficiency. Thus, the common tradeoff between efficiency and power is obtained from a first principle derivation, highlighting the quantum origins of the empirical phenomena associated with friction.

The shortcut cycle is constructed by setting the bath temperatures T_h and T_c , the minimum Rabi frequency $\Omega_{min} = \Omega_3$ and compression ratio $\mathcal{C} = \Omega_1/\Omega_3$. The remainder of the cycle parameters are then determined by the condition that the working medium is at equilibrium with the bath at the four corners of the cycle, see Figure 8a. This condition implies the relations $\Omega_4 T_h = \Omega_1 T_c$ and $\Omega_2 T_c = \Omega_3 T_h$; cycle parameters are given in Table 1. In contrast to the ideal Carnot cycle, the strokes, including exchange of energy with the bath, are denoted as open-expansion and open-compression. This change in nomenclature highlights the fact that, during these strokes, the qubit constitutes an open quantum system and at intermediate times along the strokes, the qubit is in a non-equilibrium state.

The adiabats (unitary strokes) are accelerated by employing shortcuts to adiabaticity (STA) protocols, characterized by a constant adiabatic parameter μ , see Section 4.3. The dynamics of these protocols are governed by the propagator $\Lambda_{uni} = \mathcal{U}_1 \mathcal{U}_2$ given in Equations (40) and (41). The shortcuts to adiabaticity protocols are then achieved by setting the stroke duration τ such that \mathcal{U}_2 is proportional to the identity. The net effect for an initial state with no coherence is a total scaling of the energy. This is achieved for τ , satisfying $\kappa\theta(\tau) = 2\pi l$, with $l \in \mathbb{N}$ Equation (41). In the following analysis, we choose $l = 1$, Equation (47).

Other STA protocols are possible; nevertheless, the specific choice of an STA protocol only slightly affects the qualitative thermodynamic cycle performance. Different STA protocols lead to the same state-to-state transformation, while generating different transient dynamics and having different stroke durations. In principle, if the energy of the driving is not bounded, then one can achieve the adiabats in vanishing time by utilizing the bang-bang protocols, Section 4.3. The net effect of different stroke duration is therefore just an additional constant to the cycle time. Overall, the qualitative thermodynamic performance is determined by the isothermal protocols. We present the description of the chosen STA protocol for the sake of completeness.

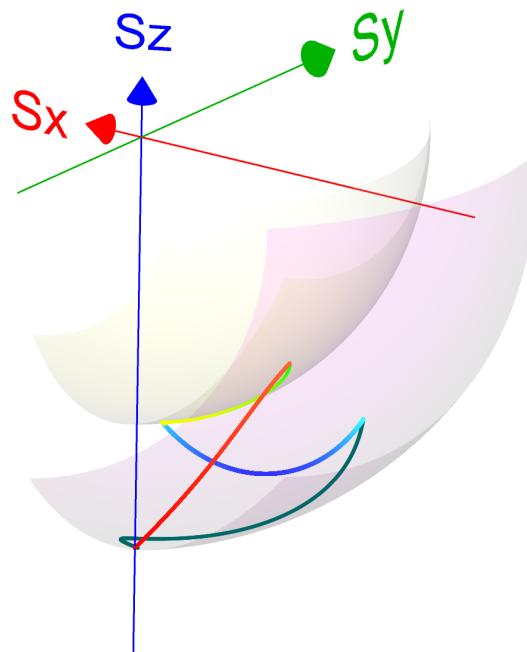


Figure 7. Shortcut Carnot cycle: Polarization change during the four strokes. The two hemispheres represent constant polarization for the two unitary strokes. The red part of the cycle trajectory is the hot isotherm connecting the two constant polarization hemispheres. The blue section is the cold isotherm. Green sections represent adiabats, where the the top curve corresponds to the expansion stroke and the bottom curve to the compression.

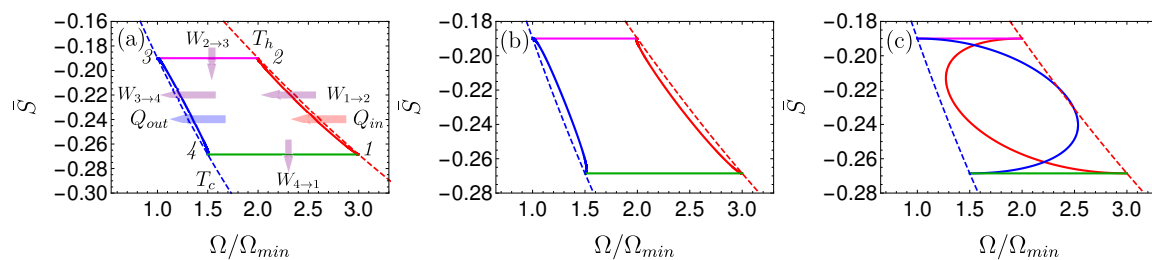


Figure 8. Shortcut Carnot cycle: Polarization as a function of the Rabi frequency for the four different cycle duration's: (a) $\tau_{cyc} = 192$ (b) $\tau_{cyc} = 108$ (c) $\tau_{cyc} = 9$, units of $(2\pi/\Omega_{min})$, with $\Omega_{min} = \Omega_3$ m.u. (model units $\hbar = k_B = c = 1$). The hot and cold isotherms are represented by dashed red and blue lines and the cycle points are denoted by numbers. Incoming (outgoing) arrows designate consumption (extraction) of work or transfer of heat to (from) the qubit. For slow driving, the cycle lies close to the reversible Carnot cycle, Panel (a). Increasing the driving speed leads to dissipation and deviations from reversible operation, Panel (b). Eventually, below a the transition cycle time $\tau_{trans} = 12.7 (2\pi/\Omega_{min})$, the cycle transitions to a dissipator operation mode, Panel (c). Table 1 summarizes the cycle parameters.

The acceleration of the open-strokes is obtained by employing STE protocols, which are described in detail in Section 5.3. The speedup relies on non-adiabatic dynamics and the generation of coherence at intermediate times. The STE protocols are engineered in order to incorporate both the unitary effect, which leads to rise in coherence, and the dissipative interaction that induces decay of coherence. These two contributions are combined to induce conversion of all the coherence of the working medium to energy at the final stage of the protocol. When the driving is slow, only a small amount of coherence is generated and the evolution is close to an isothermal process. The close proximity of the polarization during the open-strokes is observed in Figure 8a (dashed lines).

Accelerating the driving generates larger coherence accompanied by a thermodynamic cost. This link between coherence and thermodynamic cost follows from the properties of the dynamical propagator at constant μ , Equation (41). During the open-strokes, the coupling to the bath leads to the decay of coherence. This decay increases with the amount of coherence present. As a result, rapid driving leads to enhanced dissipation, which reduces the cycle performance.

Figure 8 shows a visual representation of this phenomenon, which compares three Carnot-type cycles with varying cycle times. The amount of extracted work during a single cycle is related to the area enclosed by the $\bar{S}(\Omega)$ plot. As the cycle time decreases, the open-strokes deviate further from the isotherms (Panel b), consuming more work and dissipating larger amounts of energy and coherence. Figure 9 shows the entropy production rate on the open strokes for these cycles. At the beginning and the end of the stroke, the entropy production rate Equation (64) is zero, since the protocol is designed to reach equilibrium on the four corners of the cycle. The area under the lines is the total entropy production. As expected, the entropy production increases for decreasing stroke duration. Eventually, the cycle transitions to an accelerator operation mode, where work is consumed during both open-strokes (Figure 8c), which enhances the entropy production.

In the opposing limit of long cycle times, the dynamics are adiabatic and the efficiency approaches the Carnot efficiency η_C , Figure 10. The improved efficiency is obtained on account of a reduction in power, see Figure 11. Optimal power is obtained for relatively short cycle times $\tau_{cyc} \approx 24 (2\pi/\Omega_{min})$ for the Carnot type cycle and a shorter time of $\tau_{cyc} \approx 11 (2\pi/\Omega_{min})$ for the Otto cycle. Overall, the power of the shortcut Carnot cycle exceeds the local Otto cycle for almost all cycle times. Figure 12 shows the typical efficiency-power tradeoff for the shortcut Carnot cycle. The plot is compatible with the tradeoff bound in [108,109] (given by dashed purple and green lines), applicable to the low dissipation case. Two bounds are presented, the first, given by the expression: $\frac{\eta}{\eta_C} + \frac{(1-\eta_C)(\mathcal{P}/\mathcal{P}_{max})}{2(1+\sqrt{1-(\mathcal{P}/\mathcal{P}_{max})})-\eta_C(\mathcal{P}/\mathcal{P}_{max})} \leq 1$, corresponds for efficiencies past the efficiency at maximum power (right bound—dashed green line), while the second line corresponds $2(\eta/\eta_C) + \sqrt{1-(\mathcal{P}/\mathcal{P}_{max})} \geq 1$ (left bound—dashed orange line). Notice that the value of the normalized efficiency η/η_C for $\mathcal{P}/\mathcal{P}_{max} = 1$ is different for the right and left bounds. This emerges from the fact that the right bound depends explicitly on the Carnot efficiency, while the left bound only depends on the normalized ratio.

Surprisingly, when comparing the two different protocols for the angle ϕ (see below Equation (63)), the performance of the cycle is almost independent of the chosen protocol for ϕ . The primary difference between the two cycles concerns the amount of coherence that are generated during the open-strokes. As expected the protocol which includes a rotation of $\pi/2$ in ϕ exhibits much larger coherence along the stroke. We expect that, for higher values of μ , protocols that are characterized by a rotation of the Hamiltonian will generate more coherence. In turn, this will shift the point of transition from an engine to an accelerator to larger cycle times.

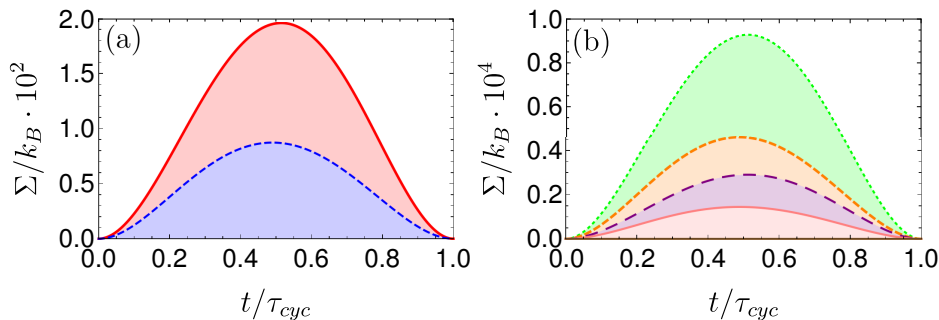


Figure 9. Entropy production rate for the open strokes of the shortcut Carnot cycle as a function of normalized time for various cycle times. Panel (a): Open-compression (red) and open-expansion (dashed blue) for a short cycle time $\tau_{cyc} = 9(2\pi/\Omega_{min})$. Panel (b): Open-compression (dotted green/dashed purple) and open-expansion (dashed orange/continuous pink) for a large cycle time $\tau_{cyc} = 108/192(2\pi/\Omega_{min})$. The three cycle times correspond to the cycles that are plotted in Figure 8. Decreasing the cycle time increases the dissipation and results in a greater entropy production. The compression strokes include cooling the qubit, which requires greater amounts of entropy production relative to the open-expansion strokes for the same stroke times.

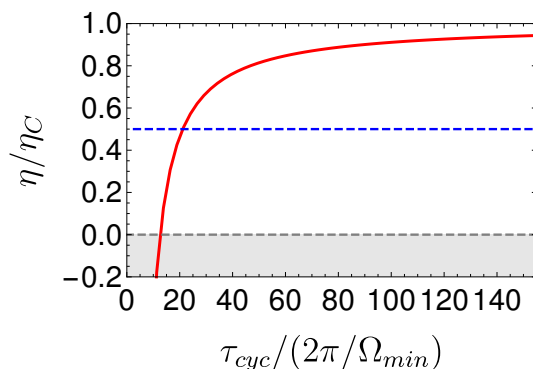


Figure 10. Normalized efficiency as a function of the cycle time for a local Carnot cycle (thick red) and local Otto cycle (blue dashed). In the local Carnot cycle long cycle times lead to close to reversible dynamics, optimizing the efficiency towards the Carnot bound η_C . For short cycle times dissipation of energy and coherence leads to a degradation of efficiency. Eventually, resulting in a transition from an engine operation mode ($\eta \equiv -W/Q_h > 0$) to an accelerator operation mode ($\eta < 0$). The two studied protocols for the angle $\phi(t)$ (below Equation (63)) cannot be distinguished in this graph. In the local Otto cycle, the efficiency $\eta_{Otto} = 1 - \Omega_c/\Omega_h$ is independent of the cycle time.

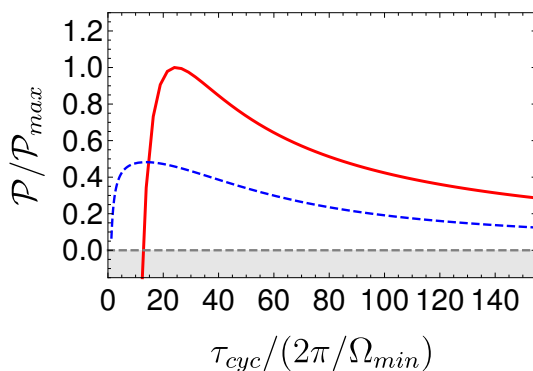


Figure 11. Power as a function of cycle time for a local Carnot cycle (red thick line) and local Otto cycle (blue dashed line). Slow driving leads to a reduction in power $\mathcal{P} \equiv -W/\tau_{cyc}$. Moreover, under rapid driving dissipation reduces the net extracted work, leading to an optimal power of $\mathcal{P}_{max} = 5.19 \times 10^{-3}$ m.u. for $\tau_{cyc} \approx 24(2\pi/\Omega_{min})$ for the local Carnot and $\mathcal{P}_{max} = 2.5 \times 10^{-3}$ m.u. for $\tau_{cyc} \approx (2\pi/\Omega_{min})$ for the local Otto cycle.

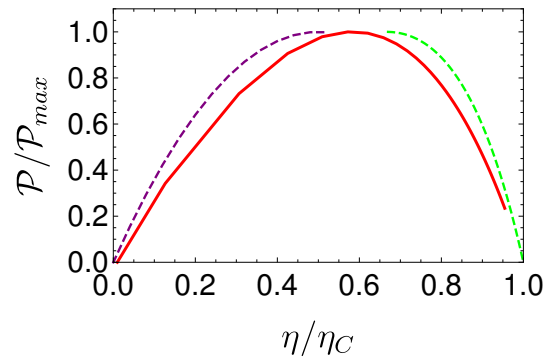


Figure 12. Power as a function of efficiency for the local Carnot cycle (red continuous line) and upper bounds (dashed purple and green lines) [108]. The typical behavior is a manifestation of the tradeoff between efficiency and power. The efficiency at maximum power $\eta_{\max \mathcal{P}} \approx 0.57$ exceeds the Curzon–Ahlborn efficiency $\eta_{CA} = 1 - \sqrt{T_c/T_h} \approx 0.3$. This result is not surprising, as the operation speed goes beyond the low dissipation regime [66].

7. Global Cycles

Closing globally coherent cycles requires more than just connecting the four strokes, since the four corners of our cycle are no longer required to be Gibbs states. In general, we prescribe a periodic driving protocol and the qubit is thereby driven to a limit cycle [76].

We will start by examining the Otto cycle which is easier to analyze. Figure 13 shows an example of a global Otto cycle. During the unitary strokes of the Otto cycle, $\Lambda_{h \rightarrow c}$ and $\Lambda_{c \rightarrow h}$, non-adiabatic dynamics generates coherence, which carries the system away from the energy direction [74,110,111]. This coherence subsequently decays during the isochoric strokes. Note that, if STA protocols are used on the unitary strokes, then no coherence ever dissipates, leading to no friction, and the discussion from the frictionless treatment in Sections 3.3 and 3.4 applies. Because our goal is to understand the behavior, including friction, we use constant μ protocols for the unitary strokes. These are only frictionless for quantized stroke durations. We present results for the power and the efficiency as a function of the cycle time. Because our STA protocols are only frictionless for quantized times, the behavior in Figures 15 and 16 shows oscillations for cycle times smaller than $\tau (l = 1)$. Interestingly, except for some wild oscillations for very small times, the power of the coherent Otto cycle is monotonically decreasing in the cycle time, reaching its maximum for the sudden cycle in the limit of $\tau \rightarrow 0$ for small Φ . Therefore, we begin with a closer look at this case.

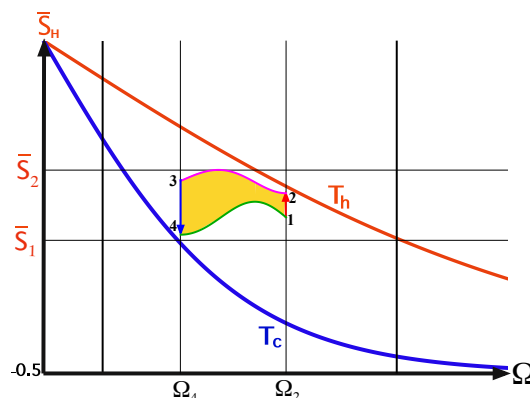


Figure 13. Global Otto cycle with friction. Projection of the polarization on the energy axis as a function of the generalized Rabi frequency. The coherence at the end of the adiabats dissipates during the isochores. Because of the decay of this coherence, the polarization along the adiabats always exceeds its initial value. In the presented cycle $\mu > \mu_{l=1}$.

7.1. Global Otto Cycle and the Sudden Limit

We now analyze the influence of coherence in the sudden limit. In general, the working medium Hamiltonian $\hat{H}(t)$, Equation (2), does not commute with itself at different times, generating substantial coherence under rapid driving. As will be demonstrated, this coherence has a direct effect on the thermodynamic performance and the cycle's operation mode.

The sudden operation is characterized by only two types of strokes: unitaries and isochores. When the Hamiltonian parameters are instantaneously varied, the working medium dynamics is dominated by the unitary part (adiabats). Any finite coupling with the bath (weak in our analysis) only negligibly affects the working medium state. During the isochores, the control parameters remain constant and a small amount of heat transfer occurs. Note that the initial portion of an isochore has the largest temperature difference between the bath and our qubit, so the sudden cycle only uses this fastest heat exchange, explaining how the power can be maximum in the zero time limit.

As in the general case, the evolution of the working medium during the sudden Otto cycle is constructed by combining the propagators of the adiabats $\Lambda_{i \rightarrow f}^{sudd}$, Equation (43), and the propagators for the isochores Λ_{sudd}^{iso} . The propagators for the isochores are obtained by substituting the basis operators $\{\hat{H}, \hat{L}, \hat{C}, \hat{I}\}$ into the Heisenberg form of the master equation, Equation (14), and expanding the solution up to first order in the stroke time τ . This leads to

$$\Lambda_i^{sudd} = \begin{bmatrix} 1 - \Gamma_i \tau & 0 & 0 & \Gamma_i \tau \Omega_i \langle \bar{S}_{eq}(\Omega_i, T_i) \rangle \\ 0 & 1 - \Gamma_i \tau / 2 & -\Omega_i \tau & 0 \\ 0 & \Omega_i \tau & 1 - \Gamma_i \tau / 2 & 0 \\ 0 & 0 & 0 & 1 \end{bmatrix}, \quad (75)$$

where $i = h, c$ indicates the frequency of the hot and cold baths. In the studied sudden Otto cycle $\Omega_{h/c} = \Omega_{2/4}$ and the kinetic rates are taken to be equal $\Gamma_i = \Gamma_c = \Gamma_h$. Concatenating the stroke propagators in the suitable order generates the sudden cycle propagator

$$\Lambda_{cyc}^{sudd} = \Lambda_{c \rightarrow h}^{sudd} \Lambda_c^{sudd} \Lambda_{h \rightarrow c}^{sudd} \Lambda_h^{sudd}. \quad (76)$$

Next, we solve for the invariant of the limit cycle $\Lambda_{cyc}^{sudd} \vec{v} = \vec{v}$, where the elements of \vec{v} give the expectation values of the basis operators $\{\hat{H}, \hat{L}, \hat{C}\}$ at the beginning of the hot isochore. This information is sufficient for determining the qubits state throughout the cycle and, in turn, allow evaluating the thermodynamic quantities.

We find that in the sudden limit, the cycle's performance is highly sensitive to the coherence generation along the adiabats. The amount of accumulated coherence is determined by the relative phase Φ , see Equation (43). For $\Phi = 2\pi k$, $k \in \mathbb{Z}$, the Hamiltonian commutes with itself at different times and the state remains diagonal in the energy basis. In contrast, for intermediate values of Φ , coherence builds up along the adiabats and dissipates during the isochores. The dissipation leads to a reduction in power and efficiency. We find that, in the sudden limit, the extraction of power is only obtained for small amounts of coherence. This regime corresponds to phase values close to $\Phi = 2\pi k$, see Figure 14a. It is important to note that the generated coherence on a unitary stroke is employed to reduce the work against friction in the consecutive unitary stroke. Eliminating this coherence on the isochores will transform the engine into a dissipator.

It is convenient to characterize the cycle performance in terms of the standard expression of efficiency: $\eta = -\mathcal{W} / \mathcal{Q}_h$. Under an engine operation mode, the efficiency remains within the range $0 \leq \eta \leq \eta_c$. With increasing coherence generation (increasing Φ), the dissipated work exceeds the extracted work, leading to a net positive work. In this operation regime work is consumed ($\mathcal{W} > 0$), while heat keeps flowing from the hot bath to the cold bath ($\mathcal{Q}_h > 0, \mathcal{Q}_c < 0$). Thus, η becomes negative, see Figure 14b. When further increasing the coherence generation, the qubit starts dissipating energy to both baths ($\mathcal{Q}_c, \mathcal{Q}_h < 0$); this implies that η changes its sign abruptly and becomes positive.

The maximum coherence generation is achieved for $\Phi = \pi k$, which corresponds to an equal magnitude of the x and z components of the Hamiltonian (cf. Section 3.4).

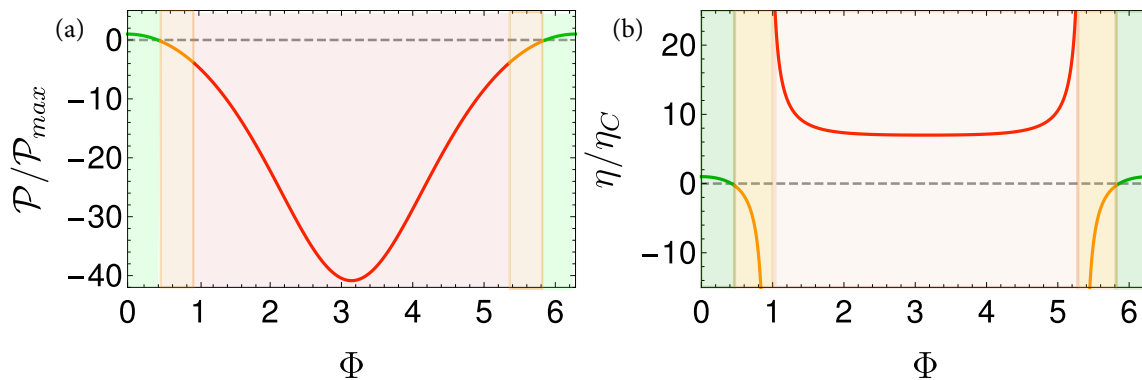


Figure 14. (a) Normalized power and (b) efficiency as a function of the relative phase Φ . When the phase values are near $2\pi k$, $k \in \mathbb{Z}$, only small amounts of coherence are generated and the cycle operates as an engine (green lines), which produces a positive power output. Once the phase deviates from the optimal values, the net work becomes positive and the cycle operates as an accelerator (orange lines, $\mathcal{W} > 0$, $\mathcal{Q}_h > 0$, $\mathcal{Q}_c < 0$), accelerating the flow from hot to cold. When the coherence generated during the adiabats dissipates to both baths on the isochores, the cycle transitions to a dissipator $\eta > 1$ (red line, $\mathcal{Q}_c, \mathcal{Q}_h < 0$, $\mathcal{W} > 0$). The model parameters are: $T_c = 5$, $T_h = 10$, $\Omega_c = 6$, $\Omega_h = 8$, $\Gamma_h \tau_h = \Gamma_c \tau_c = 0.01$, where τ_h and τ_c are the stroke durations of the hot and cold isochores.

The isochores include off-diagonal terms ($\propto \Omega_i \tau$), which couple the coherence operators \hat{L} and \hat{C} . This coupling originates from the unitary contribution to the open-system dynamics, (the unitary term is of the form $\frac{i}{\hbar} [\hat{H}, \hat{X}]$ in the Heisenberg equation of motion for the operator \hat{X}), and tends to complicate the solution by coupling the dynamics of all three operators along a complete cycle. In practice, we find that this coupling only slightly affects the results, improving the power by a very small amount ($\sim 10^{-2} \mathcal{P}_{max}$). This typical behavior justifies discarding the coupling terms when evaluating the efficiency and power. Without these terms, their expressions in the sudden limit ($\tau_{cyc} \rightarrow 0$) read

$$\eta = \left(8c_\Phi \Omega_h \Omega_c \left(\bar{S}_{eq}^c \Omega_h + \bar{S}_{eq}^h \Omega_c \right) - \Omega_c \Omega_h \left(\Omega_h \bar{S}_{eq}^h + \Omega_c \bar{S}_{eq}^c \right) \right) (c_{2\Phi} + 7) / G \tag{77}$$

$$\mathcal{P} = \frac{\Gamma \left(8c_\Phi \left(\bar{S}_{eq}^c \Omega_h + \bar{S}_{eq}^h \Omega_c \right) - \left(\Omega_c \bar{S}_{eq}^c + \Omega_h \bar{S}_{eq}^h \right) (c_{2\Phi} + 7) \right)}{4(c_{2\Phi} - 17)}, \tag{78}$$

with $G \equiv \Omega_h \left(8 \langle S_{eq}^c \rangle \Omega_c \Omega_h c_\Phi - \langle S_{eq}^h \rangle \Omega_h \Omega_c (c_{2\Phi} + 7) \right)$ and using the shorthand notation $c_x = \cos(x)$ and $s_x = \sin(x)$. In the evaluation of the power, we assumed equal stroke durations on all strokes.

7.2. Global Carnot-Type Constant Adiabatic Parameter Cycle

By definition, our Carnot-type cycles are constrained to be in equilibrium at switching points between two adjacent strokes. This requirement implies that coherence is only maintained “locally” within the strokes and it defines what we mean by local coherence operation of our engines. In the following analysis, we lift this restriction to study the properties of “global” coherence operation.

A globally coherent cycle is constructed from two open-strokes and two adiabats. For our implementation, the value of μ is kept constant for the entire protocol. We study the performance of the limit-cycle, which maintains coherence throughout the cycle. We reduce the compression ratio \mathcal{C} of the cycle while maintaining the same bath temperatures in order to produce power. Two globally coherent Carnot cycles are studied, which differ by the inner frequencies of the cycle, Ω_2 and Ω_4 . The frequencies are chosen to fit an endoreversible Carnot cycle with a constant temperature gap, in the

first cycle $\Delta T_h = \Delta T_c = 1$ m.u. and for the second cycle $\Delta T_h = \Delta T_c = 2$ m.u. Table 1 summarizes the cycle parameters. These cycles maintain a non-vanishing heat flow in the desired direction on the open-strokes.

The protocol choice of a constant adiabatic parameter allows for an additional degree of freedom in the choice of the Hamiltonian controls $\omega(t)$ and $\epsilon(t)$. We choose to set them, as in Equation (62). We then obtain a relation between the phase and Rabi frequency: $\Omega(t) = -\dot{\phi}/\mu$. For small $\dot{\phi}$, the protocols can be very rapidly achieved while keeping μ small, thus still maintaining quantum adiabatic evolution. However, in such regime a slow change in the phase implies that $\omega(t)$ and $\epsilon(t)$ are nearly proportionate to one another, resulting in a Hamiltonian that commutes with itself at different times. In order to study the influence of coherence on the thermodynamic performance, we require a substantial change in phase. For this reason, we determine the driving protocols by setting both initial and final Rabi frequencies, Ω_i and Ω_f and phases ϕ_i and ϕ_f . In the quantitative analysis, we choose $\Phi = \phi_f - \phi_i = \pi/2$, meaning that the Hamiltonian direction rotates from the z to the x axis during the open-expansion stroke ($-\pi/2$ on the open-compression stroke).

Global coherence operation allows for coherence, generated in one stroke, to be converted to energy and utilized during the adjacent strokes. Accelerating the driving enhances this phenomenon by generating greater coherence, which eventually dominates the cycle's performance. Using the coherence measure \mathfrak{C} , Equation (34), we observe that, when $\mathfrak{C} > 0.01$, relative to a maximum value of 0.5, strong interference takes place, which are manifested in oscillations in power and efficiency. The coherence value should also be compared to the typical value of $|\bar{S}_H|$, which is of the order ≈ 0.1 . Figure 15 presents the scaled efficiency for varying cycle times. In the slow driving regime, coherence only degrades the extracted work and efficiency increases monotonically with the cycle time. In contrast, for sufficiently fast driving, the efficiency oscillates rapidly due to interference. If the generated coherence is utilized efficiently, the cycle extracts more work and the efficiency improves. Moreover, optimal power is obtained in the fast driving regime, as in Figure 16.

On the other hand, if generation and consumption of coherence is not coordinated with the stroke times (related to the cycle time), the dissipation increases, which decreases the efficiency. Overall, the oscillations in efficiency constitute a signature of a quantum operation mode [75], dominated by coherence.

Generally, the efficiency at long cycle durations surpasses the local optima seen at short cycle times. This is a consequence of strong dissipation of coherence under rapid driving. Even when the generation and consumption of coherence is fully coordinated with the stroke duration, a still greater amount of coherence leads to greater dissipation on the open strokes and a reduction in efficiency. Therefore, no quantum advantage is expected in this scenario.

The entropy production rate of these cycles is almost constant throughout the cycle, as in Figure 17. This is a confirmation that the cycle is always far from the instantaneous attractor. Shorter cycle periods lead to larger entropy production. The breakup of entropy production to an energy like term $\Sigma_\chi = \mathcal{F}_\chi \mathcal{J}_\chi$ and a coherent part $\Sigma_{\sigma_{x/y}} = \mathcal{F}_{\sigma_{x/y}} \mathcal{J}_{\sigma_{x/y}}$, Section 5.4, show similar values for large μ , which means that coherence dominates the cycle. For small μ (large cycle times), the entropy production is dominated by Σ_χ , which can be attributed to irreversible heat transport.

In the asymptotic limit (large τ_{cyc}), the working medium remains in the linear response regime during the open strokes. This regime is characterized by low dissipation and a typical $1/\tau_{cyc}$ scaling law of the dissipated energy. Similarly, one can introduce the dissipated power, defined as $\mathcal{P}_{diss} = \mathcal{P} - |\mathcal{W}_{ideal}|/\tau_{cycle}$, where the ideal work \mathcal{W}_{ideal} is achieved in the large time limit. In the linear response regime the dissipated power is expected to scale asymptotically as $1/\tau_{cyc}^2$ [112]. Under small μ (slow driving), the globally coherent cycle exhibits such typical behavior, as showcased in the inset of Figure 15.

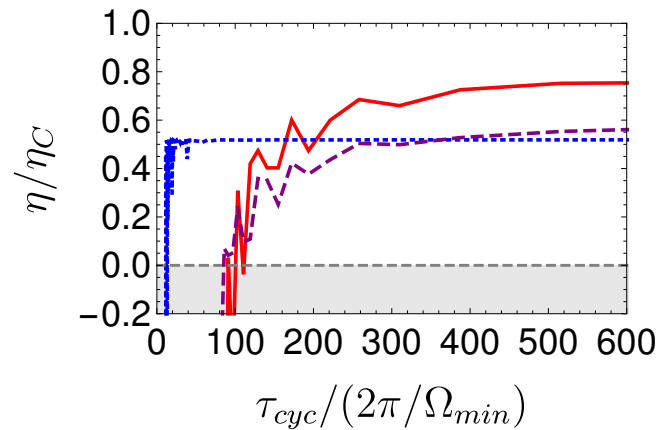


Figure 15. Normalized efficiency as a function of the cycle time for the Globally coherent Carnot (continuous red and dashed purple) and Otto cycles (dotted blue). In the slow driving regime, coherence only degrades the extracted work output and the efficiency. As the cycle time increases less coherence is generated and the efficiency increases monotonically. In the rapid driving regime, the cycle exhibits a quantum operation mode, where the cycle performance is dominated by coherence. In this driving regime, when coherence generation and consumption is coordinated with the stroke times, the cycle efficiently produces work. On the other hand, for stroke time leading to induced dissipation of coherence, the work extraction declines and the cycle may transfer to a dissipator operation mode ($\eta < 0$). This sensitivity to coherence leads to an oscillatory dependence for short cycle times. The efficiency of the Carnot-global cycle exceeds the efficiency of the global Otto cycle at long cycle times. This result stems from the reduced compression ratio of the global Otto cycle. This relative performance reverses for short cycle times. In this driving regime, the global Otto maintains a close to optimal efficiency where the Carnot cycle performance degrades and the cycle ceases to operate as an engine. For the chosen cycle parameters, the Carnot efficiency obtains a value of $\eta_C = 0.75$. The two Globally Carnot cycle differ by their Ω_2 and Ω_4 frequencies. As a result, the effective temperature gap of the purple cycle is larger compared to the red cycle. When comparing to the power plot (Figure 16), the cycle with lower efficiency exhibits a larger maximum power. The Globally coherent Carnot and global Otto cycles parameters are summarized in Tables 1 and 2.

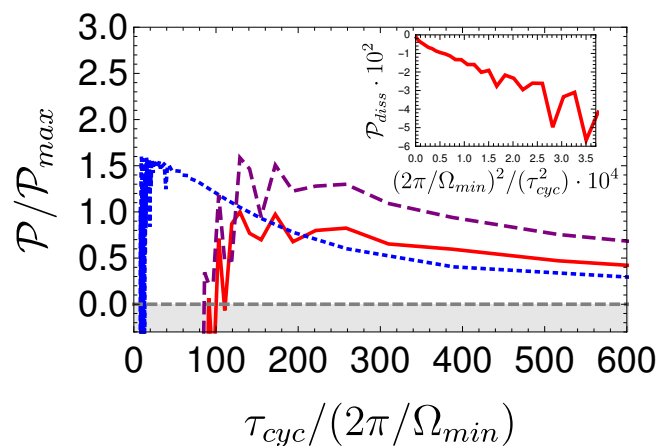


Figure 16. Power as a function of the cycle time for the Globally coherent Carnot (continuous red and dashed purple) and global Otto (dotted blue) cycles. The maximum power for the two Carnot cycles are $\mathcal{P}_{max} = 1.8 \cdot 10^{-3}$ m.u. for the purple $\mathcal{P}_{max} = 1.14 \cdot 10^{-3}$ m.u. for the red, and for the Otto $\mathcal{P}_{max} = 1.8 \cdot 10^{-3}$ m.u. Inset: Dissipated power $\mathcal{P}_{diss} = \mathcal{P} - |\mathcal{W}_{ideal}| / \tau_{cyc}$ as a function of a scaled $1/\tau_{cyc}^2$. For large cycle times, the dissipated work scales as $1/\tau_{cyc}$ and the dissipated power as $\mathcal{P}_{diss} \propto 1/\tau_{cyc}^2$. This result is in accordance with a linear response analysis. Cycle parameters are presented in Table 1.

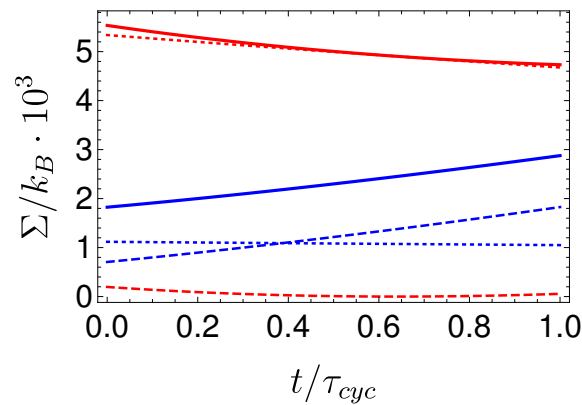


Figure 17. Entropy production rate as a function of normalized time for the Globally coherent Carnot cycle with $|\mu| = 0.3$. The total entropy production rate for the open-expansion and open-compression strokes are shown in thick red and blue lines, correspondingly. These are a sum of entropy production due to the flux of $\langle \hat{\chi} \rangle$, $\mathcal{F}_{\chi} \mathcal{J}_{\chi}$ (dashed lines), and coherence-like terms $\mathcal{F}_{\sigma_x} \mathcal{J}_{\sigma_x} + \mathcal{F}_{\sigma_y} \mathcal{J}_{\sigma_y}$ (dotted lines). The various contributions are, as expected, positive. With decreasing μ the coherence-like terms decrease and the term $\mathcal{F}_{\chi} \mathcal{J}_{\chi}$ is the dominant contribution to the entropy production. The breakup of the entropy production in the $\{\hat{H}, \hat{L}, \hat{C}\}$ basis will show a similar pattern.

We can compare the performance of the Globally coherent Carnot and Otto cycle. Both cycles maintain coherence throughout the cycle, where in the global Otto cycle coherence is generated only during the unitary strokes. The turnover to an operation mode that is strongly influenced by interference requires faster driving and larger value of coherence measure $\mathcal{L} > 0.1$. As a result, the coherent affected operation mode at shorter cycle time. This characteristic behavior can be witnessed in Figure 15. The shorter cycle times allow for the global Otto cycle to possess comparable maximum power with respect to the Globally coherent Carnot cycle with higher efficiency.

Table 1. Shortcut (local) and Globally coherent cycle parameters are given in the model units (m.u.), satisfying $\hbar = k_B = c = 1$. The parameters for the Globally Carnot cycle correspond to the continuous red line in Figures 15 and 16, while the parameters in parentheses correspond to the purple dashed lines.

Parameters	Local Carnot	Globally Coherent Carnot	Local Otto	Globally Coherent Otto
Ω_1	12	10	8	9
Ω_2	8	9 (6.857)	8	9
Ω_3	4	6	6	$6\sqrt{3}$
Ω_4	6	$6\sqrt{3}$ (8.75)	6	$6\sqrt{3}$
Hot bath temperature	$T_h = 10$	$T_h = 10$	$T_h = 10$	$T_h = 10$
Cold bath temperature	$T_c = 5$	$T_c = 5$	$T_c = 5$	$T_c = 5$

Table 2. Stroke parameters are given in the model units (m.u.), satisfying $\hbar = k_B = c = 1$.

Parameters	Value
Coupling constant $A \equiv g^2/2\hbar c$	0.01
Integration step size	10^{-3}

8. Quantum Signature: Constant Adiabatic Parameter Cycles Maintaining Global Coherence

A quantum signature is defined as a measurable quantity of the system which affirms non-classical behavior [23,113]. In the present scenario, we search for thermodynamic properties that are susceptible. Unlike classical features, quantum properties are sensitive to any measurement that extracts information on the system state. This feature allows validating the quantum signature by analyzing the affect of measurements on the cycle performance. Specifically, we compare the globally

coherent Carnot cycle efficiency to the efficiency in the presence of weak quantum measurements of energy in the instantaneous energy basis, which are performed on the unitary strokes.

The weak measurement back action effectively leads to a double commutator term $-k_d [\hat{H}, [\hat{H}, \hat{X}]]$ in the master equation for the system operator \hat{X} [114]. Such a term leads to pure dephasing with a dephasing constant k_d . We compare the effect of dephasing for different cycle times for the global Carnot cycle. For a specific cycle time, the results shows a decrease in efficiency for small dephasing constant k_d , Figure 18. This regime corresponds to weak measurements that only slightly influence the system dynamics and decrease the coherence. When the system is weakly perturbed, the dephasing only increases the dissipation and, therefore, reduces the efficiency. Beyond a critical value, stronger measurements (increasing the value of k_d) lead to an opposite effect and improve the efficiency. This result is related to the Zeno effect [115,116] and quantum lubrication [117], as continuously measuring the qubit forces it to remain on the energy shell. In return, this leads to less coherence generation and, therefore, reduced dissipation. The measurement backaction and the present thermodynamic analysis, should be taken with certain care. Once the qubit state is being monitored, it ceases to be an isolated system and the measurement may be accompanied by an additional heat transfer [118,119]. In addition, the measurement itself requires resources of work and heat. In the limit of projective measurement, the resources required become infinite [120]. The additional heat that arises from the weak measurement and the resources required were not accounted for in the present analysis.

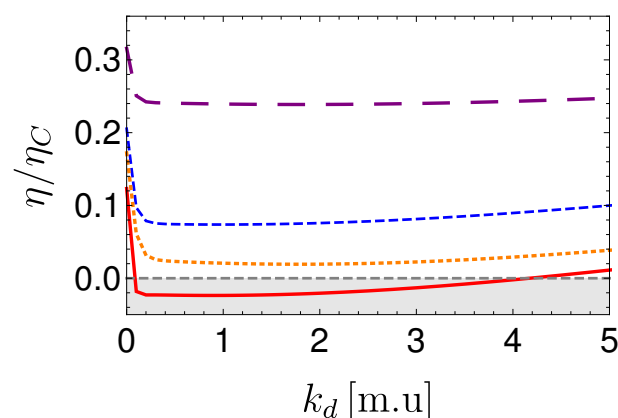


Figure 18. Efficiency as a function of dephasing constant k_d for varying cycle times for the globally coherent Carnot cycle: Red-continuous $\tau_{cyc} = 102.5$, blue dashed $\tau_{cyc} = 103$, orange dotted $\tau_{cyc} = 105$, purple long dashed $\tau_{cyc} = 129$, units of $(2\pi/\Omega_{min})$.

As expected, the influence of the measurement reduces with increasing cycle times, see Figure 18. Slower driving reduces the amount of coherence throughout the cycle, thus diminishing the affect of dephasing on the thermodynamic performance. In the quantum adiabatic limit, the system remains on the energy shell and the measurement does not disturb the system.

9. Discussion

9.1. What the Qubit Can and Cannot Do

The qubit QM model can generate expressions for thermodynamic quantities, based on first-principle derivations under the paradigm of open quantum systems. It incorporates all of the features that we expect from finite-time thermodynamics: tradeoff between efficiency and power, irreversible process, finite heat transport, friction, and heat leaks. A major advantage of the qubit model is its simplicity. Nevertheless, the model is able to elucidate the main issues of finite-time-thermodynamics, but not all types of effects. It is important to stress what phenomena we omitted from this paper, either since they deserve further study or because the model is restricted.

The present qubit model by construction is limited in describing many body effects on engine performance. For example, our model engines cannot include the entanglement in engines [121–123], engines based on many body localization as a working fluid [124], collective and critical quantum effects in engines [125–129], and synchronization [130].

In the introduction, we stated four possible sources of irreversibility; two sources that were not included in the present analysis are heat leaks and switching losses. In any realistic engine, there is always a residual system-bath coupling even during the unitary strokes [131]. As a result, additional heat currents from the hot to the cold reservoir occur. Moreover, such an interaction causes additional dephasing. These effects are not counted in our models. In addition, in all four stroke cycles presented, we ignored the energetic cost of switching the coupling to the bath, g , on and off [15,18,132,133]. Such switching occurs as the cycle transitions between unitary and open strokes. If one chooses, in Equation (11), a system bath interaction that satisfies $[\hat{H}_{s-h/c}, \hat{H}_s + \hat{H}_{h/c}] = 0$ the energetic cost of switching the coupling on vanishes. If correlations between the system and bath are generated, decoupling the system from the bath could result in an additional thermodynamic cost [132,133]. The miniaturization of engines emphasizes the role of fluctuations. Fluctuations add another twist to the tradeoff between power and efficiency [134–137]. It has recently been claimed that the possibility of heat engines to have finite power output, operate close to Carnot efficiency, and only exhibit small fluctuations is excluded [135]. For steady-state heat engines, driven by a constant temperature difference between the two heat baths, it has been claimed that, out of these three requirements, only two are compatible. The present qubit model could be a unique platform for testing these ideas [69,138].

9.2. Further Considerations

There are infinitely many thermal cycles that can operate between given hot and cold baths, and produce power. These cycles differ by the externally controlled protocols and the switching points between the strokes. Optimization can be applied to the control protocols in order to enhance power or to minimize entropy production.

In the present study, we only considered a restricted class of control strategies, and mostly emphasized control strategies that optimize individual strokes. Such control and optimization relies on the prior knowledge of the equations of motion of the working medium. The control of the qubit is based on the full $SU(2)$ algebra. This reflects the physical intuition that, in practice, the control operators do not commute in general with the system Hamiltonian. As a result, $[\hat{H}(t), \hat{H}(t')] \neq 0$.

In the unitary strokes, we explored shortcuts to adiabaticity (STA) protocols, as in Section 4.3. Without any restriction, employing STA protocols allows carrying out strokes with vanishing stroke duration. Restricting the energy or the coherence stored within the controller leads to a minimum stroke duration for frictionless operation. When analyzing the complete engine cycle, the time allocated to the unitary strokes was found to have no qualitative effect on the cycle performance.

The thermalization process during the open-strokes can be controlled as well. In the study of the Carnot-type cycles, we employed protocols that speedup the thermalization process, with the cost of additional dissipated work and concomitant entropy production. The utilized protocols achieve the target thermal state rapidly, but are by no means optimal. Thermalization strokes are a much newer development and what features might make them optimal is not yet clear. For example, it is not at all clear that our STE protocols, which cash in all of the coherence at the end of the stroke, are desirable. Cashing in this coherence before the end of the stroke may not be helpful as conversion during the following unitary stroke is easily handled. In fact, macroscopic optimizations of finite-time Carnot cycles [8] would lead to maximum energy exchange for a given entropy change of the working fluid and suggests that better use of the heat exchange time would be to utilize it fully by keeping the coherence for conversion during the following unitary stroke. Our expectation for an optimal implementation would be one that keeps the entropy production rate constant [139,140], and examining these rates in Figure 17 shows that our constant μ protocol comes reasonably close.

Besides serving as a comparison to Carnot-type cycles, our treatment of Otto cycles shows off some interesting new features. The fact that both the power and the entropy production of the cycle are proportionate to the change in polarization gives this cycle a unique character. In particular, it implies that the point of maximum power is the point of maximum entropy production, i.e., the two objectives are diametrically opposed for this engine. Some light can be shed on this situation by realizing that the thermal losses are set by the temperature gap between the qubit and the bath at their highest values at the beginning of the open strokes. After that, this gap decays, with the only control being the time spent on the stroke. This forces the heat exchange and entropy production to be the largest at the beginning of the stroke with rate decreasing with longer stroke duration.

This line of reasoning is also what led us to the closer examination of the sudden cycle for which only the very initial segment of the open branches are used. By the above line of reasoning, this initial segment is the fastest heat exchange. Using instantaneous counter-diabatic driving for the unitary strokes leads to overall frictionless operation of the sort discussed in reference [63]. The interesting feature of sudden cycles, without STAs for the unitary branches, is that instantaneous driving produces significant coherence, which is actually very useful for the cycles' performance. The unitary jumps are reversible; hence, there is no cost to going forwards and backwards and at the end we get all the invested work back [141]. The same coherence in the forward jump is used to power the backwards jump. The only difference between a forward and backward jump and sudden engine operation is the very brief stops in contact with the baths, during which some coherence decays. However, this cost in coherence is not enough to kill all the power and the sudden cycles give an important example of an engine in which coherence helps. This is contrary to conjectures in the literature that coherence is always an undesirable in heat engine operation [78]. Our findings show that this conjecture, while valid for slow operation, does not appear to be true of all types of operation; there exist valid benefits of coherence [142].

Increasing the driving increases coherence generation. On the open branches, this coherence results in rather significant frictional losses that quickly bring us to the turnover point where the friction dominates the cycle performance and the engine no longer produces work. This turnover point occurs in the Carnot cycle for much smaller values of the coherence than in the Otto cycle, presumably because, in the Carnot cycle, the open branches generate additional coherence. It is also the reason our graphs of the efficiency and the power for the Carnot cycle cannot reach lower cycle times, cf. Figures 10, 11, 15 and 16. The smooth behavior of both the efficiency and power as a function of the cycle time for local cycles gives way to oscillations at short times for global cycles (Figures 15 and 16). Coherence by nature oscillates, and these oscillations result in effectively constructive and destructive interference with the oscillation during the following stroke in our global cycles. Note that this feature also shows up for the global Otto, but at much faster cycle times. In general, the global Otto cycle is less sensitive to coherence (the coherence related operators and energy are on the same scale). While the sensitivity to coherence depends on the temperature gap between the system and bath during the open strokes; this lower sensitivity to coherence for the Otto cycle holds for any comparable gaps.

9.3. Comparing to the Harmonic Working Fluid

Engine models with the qubit and harmonic oscillator working medium have been the most popular quantum systems in the study of quantum heat devices [63,95,107,143–149]. These models share many common features, including the tradeoff between power and efficiency, and obtain the Carnot bound in the limit of large cycle time. Moreover, in the limit of low temperatures, the harmonic oscillator converges to the qubit model, and the thermodynamic performance should be equivalent. Despite the similarities, there are qualitative differences in the thermodynamic performance. The major differences between the two models can be traced to the dynamical algebra of the two, $SU(2)$ and the Heisenberg-Weyl group H_3 . The former algebra is compact, while the latter is non-compact. A direct consequence is that the heat capacity of the harmonic oscillator increases with the temperature,

saturating for high temperatures. In contrast, the capacity of the qubit reaches a maximum value and then asymptotically decreases as T^{-2} in the high temperature regime.

The different algebra influences the dynamics as well. For example, for a constant adiabatic parameter protocol (non-adiabatic driving), the effective frequency of the qubit increases, while in the harmonic case the effective frequency decreases. In turn, the effective frequency determines the relaxation rate towards the instantaneous attractor. In both models, this rate increases monotonically with the effective frequency, and the relaxation rate will be influenced in an opposite manner. In addition, the detailed balance condition is also modified, which means the internal temperature of the qubit is reduced in the presence of non-adiabatic driving. When comparing the present global cycle to an analogous harmonic cycle [75], we find that the qubit cycle has a greater sensitivity to the presence of coherence (short cycle times). A possible explanation of this result is the shift to a lower internal temperature and higher relaxation rate, which destroys the coherence and nulls the extracted work.

In the operation of the engines, both working mediums allow for performing shortcut protocols [106] on the unitary and open strokes. For frictionless and shortcut cycles, the harmonic Otto cycle exhibits a maximum efficiency when optimizing the compression ratio, which corresponds to the classical endoreversible result η_{CA} , Equation (22) [95,107]. This result is independent of the power of the engine. In contrast, the qubit model reaches the Curzon–Ahlborn efficiency for an endoreversible cycle in the high temperature limit, Section 3.2 [64].

9.4. High Temperature Limit

With the motto of learning from example, we can employ the qubit model to elucidate the path from the quantum first principle derivation to the classical FTT results. The key is the high temperature limit. This means that the polarization $|\bar{S}|$ is small and it can be used to expand the thermodynamical expressions to first order. In the elementary Carnot-type cycle this expansion leads to the Curzon–Ahlborn efficiency at maximum power η_{CA} , Equation (50), without relying on the linear Newtonian heat transfer law or the low dissipation limit [67,68,78]. If we consider the cost of driving (Section 5.4), we find that the entropy production rate Σ^u at the high temperature limit can be cast into the template of the Onsager relations, Equation (71).

The qubit engine model operates in the low dissipation limit when the cycle period is very large. We observe the expected limit (insert of Figure 16), as the dissipated power scales inversely with the square of the cycle period $\mathcal{P}_{diss} \propto 1/\tau_{cyc}^2$. This is generically true, as discussed in the next subsection.

9.5. Dissipation

The problem of operating a heat engine while trying to minimize dissipation has a simple general answer: turn off the engine so nothing happens. This, of course, has a dissipation cost of zero; you cannot do better. In order to get an interesting answer to the minimum entropy production question, we have to require something to happen. For a heat engine, one natural choice is to carry entropy ΔS from the hot bath at temperature T_h to the cold bath at temperature T_c . Once such a constraint is specified, the interesting optimizations for a finite-time heat engine range from minimum entropy production to maximum power, with maximum efficiency as merely an intermediate point [8].

The low dissipation limit has been recently employed to bound the dissipation in a heat engine while using the notion of thermodynamic distance [60,78,150]. This distance, defined on thermodynamic states using the second derivative of the entropy, bounds the finite-time cost of driving a system along a given trajectory in the linear response regime, i.e., the slow process limit. In fact the minimum cost of driving a system with relaxation time τ_R along a path of length \mathcal{L} in time τ is $\tau_R \mathcal{L}^2 / \tau$. Applied to our engine, when the qubit traces the cycle of length \mathcal{L} , the dissipated power for slow processes must be at least $\tau_R \mathcal{L}^2 / \tau^2$ as matching our observations, cf. Figure 12. How to geometrically bound the dissipation in the context of our non-adiabatic master equation formalism for

faster driving is not clear. A major difference is the coupling of energy and coherence. This issue is left for future efforts.

9.6. Experimental Connections

Realization of engines with a working medium composed of an ensemble of spins is an expected development, such as in an NMR experiment [151]. The surprise is the ability to operate an engine with a single spin.

The experimental realization of single qubit engines and refrigerators is in the process of rapid development. In part, this progress is part of a larger effort in developing quantum technology. This breakthrough is due to the ability to cool the ambient environment to temperatures in the range, or colder than, the qubit energy gap [152]. Moreover, the rapid progress in manipulations, designed for quantum information processing, can be employed for the unitary strokes of quantum heat engines. Recently, experimental realizations of four-stroke cycles were demonstrated [42–44] as well as a two-stroke engine [153]. Another application for quantum engines is in quantum sensing and in particular, thermometry. Suggestions that are based on the transition point between a quantum engine cycle and a refrigerator have recently been proposed [154–157].

A more immediate goal is quantum refrigeration [152,158]. Because any quantum device operates in ultracold temperatures, the drive for miniaturization will require an on-the-chip quantum refrigerator replacing the cumbersome dilution refrigerators of today.

10. Conclusions

The qubit thermal engine has been a source of insight concerning finite-time thermodynamics for 30 years, with its origins dating back to a time when qubits were still two-level-systems. Among the lessons from the model was the role of coherence in friction, like phenomena, in the unitary strokes. Further analysis revealed that the generation of coherence occurs on the unitary strokes and is separated from its dissipation, which occurs when the qubit is in contact with the thermal bath. This insight led first to the notion of quantum friction and later to the exploration of shortcuts to adiabaticity (STA). The analysis of the qubit engine generated a unifying overview of these finite-time thermodynamic phenomena. We have tried to present such an overview alongside our new findings.

Our study explores a new chapter in the behavior of the qubit: the study of a driven isothermal process. Recent progress in open system dynamics allowed for the treatment of thermalization processes, driven processes with time dependent Hamiltonians in contact with a heat bath [34,91,99]. This allowed for the Carnot cycle to be analyzed for shorter times than the previous linear response treatments.

This breakthrough was achieved by using a basis of eigenvectors of the instantaneous propagator of the system dynamics in the interaction representation while exploiting the dynamical $SU(2)$ algebra of the qubit. The key to the breakthrough was the non-adiabatic master equation (NAME) [34] that could correctly describe the dynamics of thermalization in a thermodynamically consistent way and eliminate issues of time reordering [99]. In the qubit model, the instantaneous attractor is rotated from the energy direction by an amount that depends on the speed of the driving and it reveals the details of the coupling between energy and coherence.

In the present manuscript, we have analyzed local cycles where the coherence is required to vanish at the switching points between strokes as well as global cycles where coherence is set only by the driving protocols and it is carried from one stroke to the next. For local cycles we designed and implemented an STE protocol that mimics an isotherm. For the global cycles we used only constant adiabatic parameter μ trajectories. Both these types of cycles are analyzed and compared. As a result, for the qubit engine we are now able to assess the role of coherence along the isothermal strokes. The global cycles exhibit oscillations in their efficiency and power once we reach small cycle times (fast driving). These oscillations are due to the oscillations in coherence and how the timing of the switching between strokes happens to catch the coherence oscillation of the previous stroke.

The Carnot-like cycles show enhanced sensitivity to coherence. This coherence can be reduced by weak measurement of the energy causing pure dephasing. Dephasing is damaging for short cycles periods, but it can be beneficial for intermediate cycle times. Another coherence related finding concerns the global Otto cycle in the sudden limit near which the coherence of the engine acts as a useful flywheel.

Our analysis calculates the entropy production rate from first principles. Using inertial coordinates for the qubit, we generally find that this entropy production naturally takes a flux-times-force form. In the high temperature limit, we find a linear relation between these fluxes and forces and an associated Onsager relation.

The present manuscript managed to compare the known behavior of local and global Otto and Carnot-like cycles. That is a lot to compare. We tried to focus on the new emergent phenomena in a coherent Carnot-type cycle. We found that, to discuss these phenomena, we needed a backdrop of related results to compare to. The above attempted synthesis is the outcome.

Author Contributions: This study is a chapter in a 25 year collaboration between P.S. and R.K., initiated by the study of an Otto spin engine with Tova Feldmann and Eitan Geva [63]. The focus on the Carnot cycle was inspired by a comment by Peter during a visit to Jerusalem, pointing out a discrepancy in the quantum heat engine studies between the many studies of Otto cycles and the few studies of Carnot and other cycles. The reason was the lack of an adequate thermodynamically consistent master equation for the isothermal strokes. It took four years to address the issue. The first step is the development of the non adiabatic master equation by R.D. and Amikam Levy [34]. R.D. continued the development setting it on firm theoretical grounds with the inertial theorem. Returning to the original objective, a shortcut to equilibration was developed [91]. The present study incorporates a broad perspective as well as many new results on the role of coherence in entropy production in the Carnot and Otto cycles. All authors have read and agreed to the published version of the manuscript.

Funding: This research was supported by the Adams Fellowship Program of the Israel Academy of Sciences and Humanities and the Israel Science Foundation, grant number 2244/14.

Acknowledgments: We would like to thank our many contributors to this study: Tova Feldmann, Eitan Geva, Lajos Diosi, Jose P Palao, Yair Rezek, Karl Heinz Hoffmann, Amikam Levy, Raam Uzdin, James Nulton, Frank Boldt, Ander Tobalina, and Andrea Insinga.

Conflicts of Interest: The authors declare no conflict of interest.

Abbreviations

The following abbreviations are used in this manuscript:

GKLS	Gorini, Kossakowski, Linblad, Sudarshan; Master equation
CPTP	Completely Positive Trace Preserving map
NAME	Non-Adiabatic Master Equation
FEAT	Fastest Effectively Adiabatic transition
STA	Shortcut To Adiabaticity
STE	Shortcut To Equilibrium

Appendix A. Representations of the Qubit State

The qubit state can be described in many alternative ways. Each representation highlights a certain aspect of the engine. We will now summarize the different approaches and the relation between them. The basic construction relies on a set of orthogonal operators that form a closed Lie Algebra $\{\hat{A}\}$

$$[\hat{A}_i, \hat{A}_j] = \sum_k C_k^{ij} \hat{A}_k \quad (\text{A1})$$

where C_k^{ij} is the structure tensor of the algebra. The orthogonality relation:

$$\text{tr}\{\hat{A}_i^\dagger \hat{A}_j\} = \delta_{ij} , \quad (\text{A2})$$

where the identity \hat{I} is part of the set and all other operators are therefore traceless. Under these conditions the state $\hat{\rho}$ can be expanded as a linear combination of the set $\{\hat{A}_j\}$

$$\hat{\rho} = \frac{1}{N} \hat{I} + \sum_j \alpha_j \hat{A}_j, \tag{A3}$$

where $\alpha_j = \langle \hat{A}_j \rangle$ and N is the size of Hilbert space. An alternative formulation includes representing the state in terms of a generalized Gibbs state [101]:

$$\hat{\rho} = \frac{1}{Z} \exp \left(\sum_j \lambda_j \hat{A}_j \right). \tag{A4}$$

The generalized Gibbs state is the maximum entropy state subject to the constraints of the expectation value $\langle \hat{A}_j \rangle = \text{tr}\{\hat{\rho} \hat{A}_j\}$, this leads to a set of non linear equations which determines the Lagrange multipliers λ_j . The forms (A3) and (A4) are unique once the expectation values $\langle \hat{A}_j \rangle$ are known.

It is convenient to express the generalized Gibbs state as a product form [159]

$$\hat{\rho} = \frac{1}{Z} \prod_k \exp(\gamma_j \hat{A}_j). \tag{A5}$$

This form is not unique since it depends on the order of operators. Once the order is set the coefficients $\{\gamma_j\}$ are determined from the expectation values $\{\langle \hat{A}_j \rangle\}$.

Specifically, for the qubit we employ the $SU(2)$ algebra and three sets of orthogonal bases. The first basis set $\vec{s} = \{\hat{S}_x, \hat{S}_y, \hat{S}_z\}^T$ represents the static polarization, where \hat{S}_j are the spin operators with the commutation relation of the $SU(2)$ algebra $[\hat{S}_i, \hat{S}_j] = i\hbar \epsilon_{ijk} \hat{S}_k$ and $\hat{\sigma}_j$. In terms of the Pauli operators $\hat{\sigma}_j$ they are expressed as $\hat{S}_j = \frac{\hbar}{2} \hat{\sigma}_j$. An arbitrary state is expressed as a linear combination of these operators in Equation (4). A geometric interpretation uses this set as a Cartesian basis in 3D Figure 1. A time-dependent rotation around the \hat{S}_y axis leads, up to a scaling, to the dynamical basis set $\vec{v}(t) = \{\hat{H}, \hat{L}, \hat{C}\}^T$, Equation (32). The $SU(2)$ algebra in the polarization basis defines a rotation in Liouville space

$$\mathcal{R}_y(\phi) = \exp \left(\frac{i}{\hbar} [\hat{S}_y, \bullet] \phi \right) = e^{\frac{i}{\hbar} \hat{S}_y \phi} \bullet e^{-\frac{i}{\hbar} \hat{S}_y \phi}, \tag{A6}$$

and the relation between the two basis sets

$$\vec{v} = \Omega(t) \mathcal{R}_y(\phi(t)) \vec{s} \tag{A7}$$

where $\phi = \arccos(\omega/\Omega)$. The explicit dependence of $\Omega(t)$ and $\phi(t)$ means that the dynamical basis set \vec{v} is time-dependent.

In terms of the dynamical basis set, the linear form of the state Equation (33) is defined. Since the Hamiltonian \hat{H} is part of \vec{v} , it is natural to define the generalized Gibbs state

$$\hat{\rho} = \frac{1}{Z} \exp \left(-(\beta \hat{H} + \lambda \hat{L} + \gamma \hat{C}) \right) \tag{A8}$$

The standard Gibbs state is obtained when $\gamma = \lambda = 0$ then $\beta = \frac{2}{\hbar \Omega} \tanh^{-1} \left(\frac{2\langle \hat{H} \rangle}{\hbar \Omega} \right)$.

The third basis set is obtained from the eigenoperators of the free propagator $\{\hat{\chi}, \hat{\sigma}, \hat{\sigma}^\dagger\}^T$, Equation (52). In terms of this set the linear form of the state in the interaction representation is given by Equation (58). In addition, the state can be expressed in a generalized Gibbs state form

$$\bar{\rho} = Z^{-1} \exp \left(- \left(\bar{\beta} \hat{\chi} + \bar{\gamma} \hat{\sigma} + \bar{\gamma}^* \hat{\sigma}^\dagger \right) \right). \tag{A9}$$

An equivalent product form has been previously been employed in Ref. [91]

$$\tilde{\rho} = Z^{-1} e^{\tilde{\gamma}\hat{\sigma}} e^{\tilde{\beta}\hat{\chi}} e^{\tilde{\gamma}^*\hat{\sigma}^\dagger} , \tag{A10}$$

where $\tilde{Z} \equiv \tilde{Z}(t) = \text{tr}(\tilde{\rho}_S(t))$ is the partition function, with time-dependent parameters $\tilde{\gamma}(t)$ and $\tilde{\beta}$.

In Section 5.4 we modify the basis set $\vec{g} = \{\hat{\chi}, \hat{\sigma}, \hat{\sigma}^\dagger\}^T$ to a hermitian basis: $\vec{g}' = \{\hat{\chi}, \hat{\sigma}_x, \hat{\sigma}_y\}^T$ where $\hat{\sigma}_x = \frac{1}{\sqrt{2}}(\hat{\sigma} + \hat{\sigma}^\dagger)$ and $\hat{\sigma}_y = \frac{i}{\sqrt{2}}(\hat{\sigma} - \hat{\sigma}^\dagger)$. The new representation allows relating the basis \vec{v} to \vec{g} by a scaling and rotation around the \hat{L} axis (cf. Figure 1)

$$\vec{g}' = \frac{\sqrt{2}}{\hbar\Omega} \mathcal{R}_L(\xi) \vec{v} , \tag{A11}$$

where $\xi = \arccos(1/\sqrt{1+\mu^2})$ and $\mathcal{R}_L(\xi) = \exp\left(\frac{i}{\hbar\Omega}[\hat{L}, \bullet]\xi\right)$.

When studying the entropy production rate in Section 5.4 we take advantage of the form

$$\tilde{\rho} = \tilde{Z}^{-1} \exp\left(-(\tilde{\beta}\hat{\chi} + \tilde{\gamma}_x\hat{\sigma}_x + \tilde{\gamma}_y\hat{\sigma}_y)\right) . \tag{A12}$$

The $\{\tilde{\beta}, \tilde{\gamma}_x, \tilde{\gamma}_y\}$ time-dependent parameters are defined by the eigenoperators expectation values. The relations are given by

$$\langle \hat{\chi} \rangle_{int} = f(r) \tilde{\beta} ; \quad \langle \hat{\sigma}_x \rangle_{int} = f(r) \tilde{\gamma}_x ; \quad \langle \hat{\sigma}_y \rangle_{int} = f(r) \tilde{\gamma}_y , \tag{A13}$$

where $\langle \bullet \rangle = \text{tr}(\bullet \tilde{\rho})$, $f(r) = -\frac{1}{\sqrt{2}r} \tanh\left(\frac{r}{\sqrt{2}}\right)$ with $r = \sqrt{\tilde{\beta}^2 + \tilde{\gamma}_x^2 + \tilde{\gamma}_y^2}$. In the large temperature limit $f(r) \approx -\frac{1}{2}$, which leads to simple relations between the thermodynamic fluxes and forces in the classical regime. Alternatively, the parameters can be expressed in terms of the expectation values

$$\tilde{\beta} = s(k) \langle \hat{\chi} \rangle_{int} ; \quad \tilde{\gamma}_x = s(k) \langle \hat{\sigma}_x \rangle_{int} ; \quad \tilde{\gamma}_y = s(k) \langle \hat{\sigma}_y \rangle_{int} , \tag{A14}$$

where $s(k) = \log\left(\frac{1-\sqrt{2}k}{\sqrt{2}k+1}\right) / \left(\sqrt{2}k\right)$ with $k = \sqrt{\langle \hat{\sigma}_x \rangle_{int}^2 + \langle \hat{\sigma}_y \rangle_{int}^2 + \langle \hat{\chi} \rangle_{int}^2}$

Appendix B. Explicit Expressions

The transition matrix from the basis operators \vec{v} to the basis operators \vec{g} . The matrix appears in the inertial solution of the qubit, Equation (51):

$$P = \begin{bmatrix} 1 & -\mu & -\mu \\ 0 & i\kappa & -i\kappa \\ \mu & 1 & 1 \end{bmatrix} . \tag{A15}$$

Table A1. Definitions and notations summary.

Parameters	Description
$\{\hat{H}, \hat{L}, \hat{C}\}; \vec{v}$	dynamical operator basis; associated vector in Liouville space
$\{\hat{S}_x, \hat{S}_y, \hat{S}_z\}; \vec{s}$	polarization operator basis; vector in Liouville space
$\{\hat{\chi}, \hat{\sigma}, \hat{\sigma}^\dagger\}; \vec{g}$	eigenoperator basis; vector in Liouville space
$\{\hat{\chi}, \hat{\sigma}_x, \hat{\sigma}_y\}; \vec{g}'$	eigenoperator basis; vector in Liouville space
X^H	Heisenberg picture
\tilde{X}	interaction picture
ω and ϵ	control parameters
Ω	generalized Rabi frequency

Table A1. Cont.

Parameters	Description
\vec{S}	polarization vector
\bar{S}	polarization
\bar{S}_H	projection of the polarization vector on the energy axis
\bar{S}_{eq}	thermal polarization
T	bath temperature
$\{\Lambda\}$	dynamical propagators
$S_{v,n}$	von-Neumann entropy
S_H	energy entropy
σ_{cyc}^u	entropy production per cycle
Σ^u	entropy production rate
Γ	decay rate
η_C and W_C	efficiency and work of the Carnot cycle
η_i, W_i, P_i and Q_i	efficiency, work, power and heat of the i 'th cycle
μ	adiabatic parameter
κ	Inertial scaling factor
α	effective frequency
\mathfrak{C}	coherence
W_{fric}	work to counter friction
ϕ	$\arccos(\omega/\Omega)$
Φ	$\phi_a - \phi_b$
P	transformation matrix between \vec{v} and \vec{g}
D	eigenvalue matrix of the eigenoperators
T_i	effective temperatures
\mathcal{J}_y	thermodynamic fluxes
\mathcal{F}_y	thermodynamic force

References

1. Carnot, S. *Réflexions sur la Puissance Motrice du feu et sur les Machines Propres à Développer Cette Puissance*; Bachelier: Paris, France, 1824.
2. Salamon, P.; Nulton, J.; Siragusa, G.; Andersen, T.R.; Limon, A. Principles of control thermodynamics. *Energy* **2001**, *26*, 307–319. [[CrossRef](#)]
3. Andresen, B.; Berry, R.S.; Ondrechen, M.J.; Salamon, P. Thermodynamics for processes in finite time. *Acc. Chem. Res.* **1984**, *17*, 266–271. [[CrossRef](#)]
4. Andresen, B.; Salamon, P.; Berry, R.S. Thermodynamics in finite time: Extremals for imperfect heat engines. *J. Chem. Phys.* **1977**, *66*, 1571–1577. [[CrossRef](#)]
5. Hoffmann, K.H.; Burzler, J.M.; Schubert, S. Endoreversible Thermodynamics. *J. Non-Equilib. Thermodyn.* **1997**, *22*, 311–355.
6. Andresen, B. Current trends in finite-time thermodynamics. *Angew. Chem. Int. Ed.* **2011**, *50*, 2690–2704. [[CrossRef](#)]
7. Curzon, F.; Ahlborn, B. Efficiency of a Carnot engine at maximum power output. *Am. J. Phys.* **1975**, *43*, 22–24. [[CrossRef](#)]
8. Salamon, P.; Nitzan, A. Finite time optimizations of a Newton's law Carnot cycle. *J. Chem. Phys.* **1981**, *74*, 3546–3560. [[CrossRef](#)]
9. Kraus, K. General state changes in quantum theory. *Ann. Phys.* **1971**, *64*, 311–335. [[CrossRef](#)]
10. Lindblad, G. On the generators of quantum dynamical semigroups. *Commun. Math. Phys.* **1976**, *48*, 119–130. [[CrossRef](#)]
11. Gorini, V.; Kossakowski, A.; Sudarshan, E.C.G. Completely positive dynamical semigroups of N-level systems. *J. Math. Phys.* **1976**, *17*, 821–825. [[CrossRef](#)]
12. Alicki, R.; Kosloff, R. Introduction to Quantum Thermodynamics: History and Prospects. In *Thermodynamics in the Quantum Regime*; Binder, F., Correa, L.A., Gogolin, C., Anders, J., Adesso, G., Eds.; Fundamental Theories of Physics; Springer: Berlin/Heidelberg, Germany, 2018. [[CrossRef](#)]
13. Davies, E.B. Markovian master equations. *Commun. Math. Phys.* **1974**, *39*, 91–110. [[CrossRef](#)]

14. Levy, A.; Kosloff, R. The local approach to quantum transport may violate the second law of thermodynamics. *EPL Europhys. Lett.* **2014**, *107*, 20004. [[CrossRef](#)]
15. Barra, F. The thermodynamic cost of driving quantum systems by their boundaries. *Sci. Rep.* **2015**, *5*, 14873. [[CrossRef](#)]
16. Hofer, P.P.; Perarnau-Llobet, M.; Miranda, L.D.M.; Haack, G.; Silva, R.; Brask, J.B.; Brunner, N. Markovian master equations for quantum thermal machines: Local versus global approach. *New J. Phys.* **2017**, *19*, 123037. [[CrossRef](#)]
17. González, J.O.; Correa, L.A.; Nocerino, G.; Palao, J.P.; Alonso, D.; Adesso, G. Testing the validity of the ‘local’ and ‘global’ GKLS master equations on an exactly solvable model. *Open Syst. Inf. Dyn.* **2017**, *24*, 1740010. [[CrossRef](#)]
18. De Chiara, G.; Landi, G.; Hewgill, A.; Reid, B.; Ferraro, A.; Roncaglia, A.J.; Antezza, M. Reconciliation of quantum local master equations with thermodynamics. *New J. Phys.* **2018**, *20*, 113024. [[CrossRef](#)]
19. Hewgill, A.; De Chiara, G.; Imperato, A. Quantum thermodynamically consistent local master equations. *arXiv* **2020**, arXiv:2008.04742.
20. Allahverdyan, A.; Nieuwenhuizen, T.M. Extraction of work from a single thermal bath in the quantum regime. *Phys. Rev. Lett.* **2000**, *85*, 1799. [[CrossRef](#)]
21. Hilt, S.; Shabir, S.; Anders, J.; Lutz, E. Landauer’s principle in the quantum regime. *Phys. Rev. E* **2011**, *83*, 030102. [[CrossRef](#)]
22. Boukobza, E.; Ritsch, H. Breaking the Carnot limit without violating the second law: A thermodynamic analysis of off-resonant quantum light generation. *Phys. Rev. A* **2013**, *87*, 063845. [[CrossRef](#)]
23. Uzdin, R.; Levy, A.; Kosloff, R. Equivalence of quantum heat machines, and quantum-thermodynamic signatures. *Phys. Rev. X* **2015**, *5*, 031044. [[CrossRef](#)]
24. Roßnagel, J.; Abah, O.; Schmidt-Kaler, F.; Singer, K.; Lutz, E. Nanoscale heat engine beyond the Carnot limit. *Phys. Rev. Lett.* **2014**, *112*, 030602. [[CrossRef](#)]
25. Alicki, R.; Fannes, M. Entanglement boost for extractable work from ensembles of quantum batteries. *Phys. Rev. E* **2013**, *87*, 042123. [[CrossRef](#)] [[PubMed](#)]
26. Mandal, D.; Jarzynski, C. Work and information processing in a solvable model of Maxwell’s demon. *Proc. Natl. Acad. Sci. USA* **2012**, *109*, 11641–11645. [[CrossRef](#)]
27. Vidrighin, M.D.; Dahlsten, O.; Barbieri, M.; Kim, M.; Vedral, V.; Walmsley, I.A. Photonic Maxwell’s demon. *Phys. Rev. Lett.* **2016**, *116*, 050401. [[CrossRef](#)]
28. Geva, E.; Kosloff, R.; Skinner, J. On the relaxation of a two-level system driven by a strong electromagnetic field. *J. Chem. Phys.* **1995**, *102*, 8541–8561. [[CrossRef](#)]
29. Geva, E.; Kosloff, R. The quantum heat engine and heat pump: An irreversible thermodynamic analysis of the three-level amplifier. *J. Chem. Phys.* **1996**, *104*, 7681–7699. [[CrossRef](#)]
30. Correa, L.A.; Palao, J.P.; Adesso, G.; Alonso, D. Performance bound for quantum absorption refrigerators. *Phys. Rev. E* **2013**, *87*, 042131. [[CrossRef](#)]
31. Correa, L.A.; Palao, J.P.; Alonso, D.; Adesso, G. Quantum-enhanced absorption refrigerators. *Sci. Rep.* **2014**, *4*, 3949. [[CrossRef](#)] [[PubMed](#)]
32. Alicki, R.; Gelbwaser-Klimovsky, D.; Kurizki, G. Periodically driven quantum open systems: Tutorial. *arXiv* **2012**, arXiv:1205.4552.
33. Albash, T.; Boixo, S.; Lidar, D.A.; Zanardi, P. Quantum adiabatic Markovian master equations. *New J. Phys.* **2012**, *14*, 123016. [[CrossRef](#)]
34. Dann, R.; Levy, A.; Kosloff, R. Time-dependent Markovian quantum master equation. *Phys. Rev. A* **2018**, *98*, 052129. [[CrossRef](#)]
35. Kosloff, R. Quantum thermodynamics: A dynamical viewpoint. *Entropy* **2013**, *15*, 2100–2128. [[CrossRef](#)]
36. Mandelstam, L.; Tamm, I. The energy–time uncertainty relation in non-relativistic quantum mechanics. *Izv. Akad. Nauk SSSR* **1945**, *9*, 122.
37. Jones, P.J.; Kok, P. Geometric derivation of the quantum speed limit. *Phys. Rev. A* **2010**, *82*, 022107. [[CrossRef](#)]
38. Giovannetti, V.; Lloyd, S.; Maccone, L. The speed limit of quantum unitary evolution. *J. Opt. B Quantum Semiclassical Opt.* **2004**, *6*, S807. [[CrossRef](#)]
39. Del Campo, A.; Egusquiza, I.; Plenio, M.B.; Huelga, S.F. Quantum speed limits in open system dynamics. *Phys. Rev. Lett.* **2013**, *110*, 050403. [[CrossRef](#)]

40. Uzdin, R.; Kosloff, R. Speed limits in Liouville space for open quantum systems. *EPL Europhys. Lett.* **2016**, *115*, 40003. [[CrossRef](#)]
41. Funo, K.; Shiraiishi, N.; Saito, K. Speed limit for open quantum systems. *New J. Phys.* **2019**, *21*, 013006. [[CrossRef](#)]
42. von Lindenfels, D.; Gräß, O.; Schmiegelow, C.T.; Kaushal, V.; Schulz, J.; Mitchison, M.T.; Goold, J.; Schmidt-Kaler, F.; Poschinger, U.G. Spin Heat Engine Coupled to a Harmonic-Oscillator Flywheel. *Phys. Rev. Lett.* **2019**, *123*, 080602. [[CrossRef](#)]
43. Ono, K.; Shevchenko, S.; Mori, T.; Moriyama, S.; Nori, F. Analog of a quantum heat engine using a single-spin qubit. *Phys. Rev. Lett.* **2020**, *125*, 166802. [[CrossRef](#)]
44. Bouton, Q.; Nettersheim, J.; Burgardt, S.; Adam, D.; Lutz, E.; Widera, A. An endoreversible quantum heat engine driven by atomic collisions. *arXiv* **2020**, arXiv:2009.10946.
45. Bejan, A.; Kestin, J. Entropy Generation Through Heat and Fluid Flow. *J. Appl. Mech.* **1983**, *50*, 475. [[CrossRef](#)]
46. Szargut, J. International progress in second law analysis. *Energy* **1980**, *5*, 709–718. [[CrossRef](#)]
47. Gouy, M. Sur l'énergie utilisable. *J. Phys.* **1889**, *8*, 501. [[CrossRef](#)]
48. Stodola, A. *Steam and Gas Turbines*; McGraw-Hill: New York, NY, USA, 1927.
49. Feldmann, T.; Kosloff, R. Characteristics of the limit cycle of a reciprocating quantum heat engine. *Phys. Rev. E* **2004**, *70*, 046110. [[CrossRef](#)]
50. Lindblad, G. Expectations and entropy inequalities for finite quantum systems. *Commun. Math. Phys.* **1974**, *39*, 111–119. [[CrossRef](#)]
51. Feldmann, T.; Kosloff, R. Quantum four-stroke heat engine: Thermodynamic observables in a model with intrinsic friction. *Phys. Rev. E* **2003**, *68*, 016101. [[CrossRef](#)]
52. Baumgratz, T.; Cramer, M.; Plenio, M.B. Quantifying coherence. *Phys. Rev. Lett.* **2014**, *113*, 140401. [[CrossRef](#)]
53. Girolami, D. Observable Measure of Quantum Coherence in Finite Dimensional Systems. *Phys. Rev. Lett.* **2014**, *113*, 170401. [[CrossRef](#)]
54. Feldmann, T.; Kosloff, R. Transitions between refrigeration regions in extremely short quantum cycles. *Phys. Rev. E* **2016**, *93*, 052150. [[CrossRef](#)] [[PubMed](#)]
55. Lin, J. Divergence measures based on the Shannon entropy. *IEEE Trans. Inf. Theory* **1991**, *37*, 145–151. [[CrossRef](#)]
56. Breuer, H.P.; Petruccione, F. *The Theory of Open Quantum Systems*; Oxford University Press: Oxford, UK, 2002.
57. Messiah, A. *Quantum Mechanics: Translated [from the French] by J. Potter*; North-Holland: Amsterdam, The Netherlands, 1962.
58. Spohn, H.; Lebowitz, J.L. Irreversible thermodynamics for quantum systems weakly coupled to thermal reservoirs. *Adv. Chem. Phys.* **1978**, *38*, 109–142.
59. Alicki, R. The quantum open system as a model of the heat engine. *J. Phys. A Math. Gen.* **1979**, *12*, L103. [[CrossRef](#)]
60. Abiuso, P.; Miller, H.J.; Perarnau-Llobet, M.; Scandi, M. Geometric optimisation of quantum thermodynamic processes. *Entropy* **2020**, *22*, 1076. [[CrossRef](#)]
61. Seifert, U. Stochastic thermodynamics, fluctuation theorems and molecular machines. *Rep. Prog. Phys.* **2012**, *75*, 126001. [[CrossRef](#)]
62. Sekimoto, K. *Stochastic Energetics*; Springer: Berlin/Heidelberg, Germany, 2010; Volume 799.
63. Feldmann, T.; Geva, E.; Kosloff, R.; Salamon, P. Heat engines in finite time governed by master equations. *Am. J. Phys.* **1996**, *64*, 485–492. [[CrossRef](#)]
64. Geva, E.; Kosloff, R. A quantum-mechanical heat engine operating in finite time. A model consisting of spin-1/2 systems as the working fluid. *J. Chem. Phys.* **1992**, *96*, 3054–3067. [[CrossRef](#)]
65. Novikov, I. The efficiency of atomic power stations (a review). *J. Nucl. Energy (1954)* **1958**, *7*, 125–128. [[CrossRef](#)]
66. Esposito, M.; Kawai, R.; Lindenberg, K.; Van den Broeck, C. Efficiency at maximum power of low-dissipation Carnot engines. *Phys. Rev. Lett.* **2010**, *105*, 150603. [[CrossRef](#)]
67. Abiuso, P.; Perarnau-Llobet, M. Optimal cycles for low-dissipation heat engines. *Phys. Rev. Lett.* **2020**, *124*, 110606. [[CrossRef](#)] [[PubMed](#)]
68. Abiuso, P.; Giovannetti, V. Non-Markov enhancement of maximum power for quantum thermal machines. *Phys. Rev. A* **2019**, *99*, 052106. [[CrossRef](#)]

69. Erdman, P.A.; Cavina, V.; Fazio, R.; Taddei, F.; Giovannetti, V. Maximum power and corresponding efficiency for two-level heat engines and refrigerators: Optimality of fast cycles. *New J. Phys.* **2019**, *21*, 103049. [[CrossRef](#)]
70. Karimi, B.; Pekola, J. Otto refrigerator based on a superconducting qubit: Classical and quantum performance. *Phys. Rev. B* **2016**, *94*, 184503. [[CrossRef](#)]
71. Pekola, J.P.; Karimi, B.; Thomas, G.; Averin, D.V. Supremacy of incoherent sudden cycles. *Phys. Rev. B* **2019**, *100*, 085405. [[CrossRef](#)]
72. Feldmann, T.; Kosloff, R. Performance of discrete heat engines and heat pumps in finite time. *Phys. Rev. E* **2000**, *61*, 4774. [[CrossRef](#)]
73. Scully, M.O.; Zubairy, M.S.; Agarwal, G.S.; Walther, H. Extracting work from a single heat bath via vanishing quantum coherence. *Science* **2003**, *299*, 862–864. [[CrossRef](#)]
74. Francica, G.; Goold, J.; Plastina, F. Role of coherence in the nonequilibrium thermodynamics of quantum systems. *Phys. Rev. E* **2019**, *99*, 042105. [[CrossRef](#)]
75. Dann, R.; Kosloff, R. Quantum signatures in the quantum Carnot cycle. *New J. Phys.* **2020**, *22*, 013055. [[CrossRef](#)]
76. Kosloff, R.; Feldmann, T. Discrete four-stroke quantum heat engine exploring the origin of friction. *Phys. Rev. E* **2002**, *65*, 055102. [[CrossRef](#)]
77. Boldt, F.; Nulton, J.D.; Andresen, B.; Salamon, P.; Hoffmann, K.H. Casimir companion: An invariant of motion for Hamiltonian systems. *Phys. Rev. A* **2013**, *87*, 022116. [[CrossRef](#)]
78. Brandner, K.; Saito, K. Thermodynamic geometry of microscopic heat engines. *Phys. Rev. Lett.* **2020**, *124*, 040602. [[CrossRef](#)]
79. Chen, X.; Ruschhaupt, A.; Schmidt, S.; del Campo, A.; Guéry-Odelin, D.; Muga, J.G. Fast optimal frictionless atom cooling in harmonic traps: Shortcut to adiabaticity. *Phys. Rev. Lett.* **2010**, *104*, 063002. [[CrossRef](#)]
80. Guéry-Odelin, D.; Ruschhaupt, A.; Kiely, A.; Torrontegui, E.; Martínez-Garaot, S.; Muga, J.G. Shortcuts to adiabaticity: Concepts, methods, and applications. *Rev. Mod. Phys.* **2019**, *91*, 045001. [[CrossRef](#)]
81. Torrontegui, E.; Lizuain, I.; González-Resines, S.; Tobalina, A.; Ruschhaupt, A.; Kosloff, R.; Muga, J.G. Energy consumption for shortcuts to adiabaticity. *Phys. Rev. A* **2017**, *96*, 022133. [[CrossRef](#)]
82. Zheng, Y.; Campbell, S.; De Chiara, G.; Poletti, D. Cost of counterdiabatic driving and work output. *Phys. Rev. A* **2016**, *94*, 042132. [[CrossRef](#)]
83. Campbell, S.; Deffner, S. Trade-off between speed and cost in shortcuts to adiabaticity. *Phys. Rev. Lett.* **2017**, *118*, 100601. [[CrossRef](#)]
84. Abah, O.; Lutz, E. Performance of shortcut-to-adiabaticity quantum engines. *Phys. Rev. E* **2018**, *98*, 032121. [[CrossRef](#)]
85. Çakmak, B.; Müstecaplıoğlu, Ö.E. Spin quantum heat engines with shortcuts to adiabaticity. *Phys. Rev. E* **2019**, *99*, 032108. [[CrossRef](#)]
86. Boldt, F.; Hoffmann, K.; Salamon, P.; Kosloff, R. Time-optimal processes for interacting spin systems. *EPL Europhys. Lett.* **2012**, *99*, 40002. [[CrossRef](#)]
87. Boldt, F.; Salamon, P.; Hoffmann, K.H. Fastest effectively adiabatic transitions for a collection of harmonic oscillators. *J. Phys. Chem. A* **2016**, *120*, 3218–3224. [[CrossRef](#)] [[PubMed](#)]
88. Funo, K.; Lambert, N.; Karimi, B.; Pekola, J.P.; Masuyama, Y.; Nori, F. Speeding up a quantum refrigerator via counterdiabatic driving. *Phys. Rev. B* **2019**, *100*, 035407. [[CrossRef](#)]
89. Tobalina, A.; Lizuain, I.; Muga, J. Vanishing efficiency of a speeded-up ion-in-Paul-trap Otto engine. *EPL Europhys. Lett.* **2019**, *127*, 20005. [[CrossRef](#)]
90. Dann, R.; Tobalina, A.; Kosloff, R. Shortcut to equilibration of an open quantum system. *Phys. Rev. Lett.* **2019**, *122*, 250402. [[CrossRef](#)]
91. Dann, R.; Tobalina, A.; Kosloff, R. Fast route to equilibration. *Phys. Rev. A* **2020**, *101*, 052102. [[CrossRef](#)]
92. Pancotti, N.; Scandi, M.; Mitchison, M.T.; Perarnau-Llobet, M. Speed-Ups to Isothermality: Enhanced Quantum Thermal Machines through Control of the System-Bath Coupling. *Phys. Rev. X* **2020**, *10*, 031015.
93. Villazon, T.; Polkovnikov, A.; Chandran, A. Swift heat transfer by fast-forward driving in open quantum systems. *Phys. Rev. A* **2019**, *100*, 012126. [[CrossRef](#)]
94. Henrich, M.J.; Rempp, F.; Mahler, G. Quantum thermodynamic Otto machines: A spin-system approach. *Eur. Phys. J. Spec. Top.* **2007**, *151*, 157–165. [[CrossRef](#)]
95. Kosloff, R.; Rezek, Y. The quantum harmonic Otto cycle. *Entropy* **2017**, *19*, 136. [[CrossRef](#)]

96. Wu, F.; Chen, L.; Sun, F.; Wu, C. Finite-time exergoeconomic performance bound for a quantum Stirling engine. *Int. J. Eng. Sci.* **2000**, *38*, 239–247. [[CrossRef](#)]
97. Yin, Y.; Chen, L.; Wu, F. Optimal power and efficiency of quantum Stirling heat engines. *Eur. Phys. J. Plus* **2017**, *132*, 1–10. [[CrossRef](#)]
98. Dong, C.; Lefkidis, G.; Hübner, W. Magnetic quantum diesel engine in Ni 2. *Phys. Rev. B* **2013**, *88*, 214421. [[CrossRef](#)]
99. Dann, R.; Kosloff, R. The Inertial Theorem. *arXiv* **2018**, arXiv:1810.12094.
100. Scandi, M.; Miller, H.J.; Anders, J.; Perarnau-Llobet, M. Quantum work statistics close to equilibrium. *Phys. Rev. Res.* **2020**, *2*, 023377. [[CrossRef](#)]
101. Alhassid, Y.; Levine, R. Connection between the maximal entropy and the scattering theoretic analyses of collision processes. *Phys. Rev. A* **1978**, *18*, 89. [[CrossRef](#)]
102. Onsager, L. Reciprocal relations in irreversible processes. I. *Phys. Rev.* **1931**, *37*, 405. [[CrossRef](#)]
103. Onsager, L. Reciprocal relations in irreversible processes. II. *Phys. Rev.* **1931**, *38*, 2265. [[CrossRef](#)]
104. De Groot, S.R.; Mazur, P. *Non-Equilibrium Thermodynamics*; North-Holland: Amsterdam, The Netherlands, 2013.
105. Hoffmann, K.; Salamon, P.; Rezek, Y.; Kosloff, R. Time-optimal controls for frictionless cooling in harmonic traps. *EPL Europhys. Lett.* **2011**, *96*, 60015. [[CrossRef](#)]
106. Del Campo, A.; Goold, J.; Paternostro, M. More bang for your buck: Super-adiabatic quantum engines. *Sci. Rep.* **2014**, *4*, 6208. [[CrossRef](#)] [[PubMed](#)]
107. Rezek, Y.; Kosloff, R. Irreversible performance of a quantum harmonic heat engine. *New J. Phys.* **2006**, *8*, 83. [[CrossRef](#)]
108. Ma, Y.H.; Xu, D.; Dong, H.; Sun, C.P. Universal constraint for efficiency and power of a low-dissipation heat engine. *Phys. Rev. E* **2018**, *98*, 042112. [[CrossRef](#)]
109. Ryabov, A.; Holubec, V. Maximum efficiency of steady-state heat engines at arbitrary power. *Phys. Rev. E* **2016**, *93*, 050101. [[CrossRef](#)]
110. Solfanelli, A.; Falsetti, M.; Campisi, M. Nonadiabatic single-qubit quantum Otto engine. *Phys. Rev. B* **2020**, *101*, 054513. [[CrossRef](#)]
111. Alecce, A.; Galve, F.; Gullo, N.L.; Dell’Anna, L.; Plastina, F.; Zambrini, R. Quantum Otto cycle with inner friction: Finite-time and disorder effects. *New J. Phys.* **2015**, *17*, 075007. [[CrossRef](#)]
112. Ma, Y.H.; Xu, D.; Dong, H.; Sun, C.P. Optimal operating protocol to achieve efficiency at maximum power of heat engines. *Phys. Rev. E* **2018**, *98*, 022133. [[CrossRef](#)]
113. Lostaglio, M. Certifying quantum signatures in thermodynamics and metrology via contextuality of quantum linear response. *arXiv* **2020**, arXiv:2004.01213.
114. Diosi, L. Weak measurements in quantum mechanics. *arXiv* **2005**, arXiv:quant-ph/0505075.
115. Facchi, P.; Gorini, V.; Marmo, G.; Pascazio, S.; Sudarshan, E. Quantum zeno dynamics. *Phys. Lett. A* **2000**, *275*, 12–19. [[CrossRef](#)]
116. Uzdin, R.; Gasparinetti, S.; Ozeri, R.; Kosloff, R. Markovian heat sources with the smallest heat capacity. *New J. Phys.* **2018**, *20*, 063030. [[CrossRef](#)]
117. Feldmann, T.; Kosloff, R. Quantum lubrication: Suppression of friction in a first-principles four-stroke heat engine. *Phys. Rev. E* **2006**, *73*, 025107. [[CrossRef](#)]
118. Elouard, C.; Herrera-Martí, D.A.; Clusel, M.; Auffèves, A. The role of quantum measurement in stochastic thermodynamics. *Npj Quantum Inf.* **2017**, *3*, 1–10. [[CrossRef](#)]
119. Elouard, C.; Jordan, A.N. Efficient quantum measurement engines. *Phys. Rev. Lett.* **2018**, *120*, 260601. [[CrossRef](#)]
120. Guryanova, Y.; Friis, N.; Huber, M. Ideal projective measurements have infinite resource costs. *Quantum* **2020**, *4*, 222. [[CrossRef](#)]
121. Zhang, T.; Liu, W.T.; Chen, P.X.; Li, C.Z. Four-level entangled quantum heat engines. *Phys. Rev. A* **2007**, *75*, 062102. [[CrossRef](#)]
122. Wang, H.; Liu, S.; He, J. Thermal entanglement in two-atom cavity QED and the entangled quantum Otto engine. *Phys. Rev. E* **2009**, *79*, 041113. [[CrossRef](#)]
123. He, J.-Z.; He, X.; Zheng, J. Entangled quantum heat engine based on two-qubit Heisenberg XY model. *Chin. Phys. B* **2012**, *21*, 050303. [[CrossRef](#)]
124. Halpern, N.Y.; White, C.D.; Gopalakrishnan, S.; Refael, G. Quantum engine based on many-body localization. *Phys. Rev. B* **2019**, *99*, 024203. [[CrossRef](#)]

125. Hardal, A.Ü.; Müstecaplıoğlu, Ö.E. Superradiant quantum heat engine. *Sci. Rep.* **2015**, *5*, 12953. [[CrossRef](#)]
126. Campisi, M.; Fazio, R. The power of a critical heat engine. *Nat. Commun.* **2016**, *7*, 11895. [[CrossRef](#)]
127. Niedenzu, W.; Kurizki, G. Cooperative many-body enhancement of quantum thermal machine power. *New J. Phys.* **2018**, *20*, 113038. [[CrossRef](#)]
128. Mukherjee, V.; Divakaran, U.; del Campo, A. Universal finite-time thermodynamics of many-body quantum machines from Kibble-Zurek scaling. *arXiv* **2020**, arXiv:2003.06607.
129. Jaramillo, J.; Beau, M.; del Campo, A. Quantum supremacy of many-particle thermal machines. *New J. Phys.* **2016**, *18*, 075019. [[CrossRef](#)]
130. Jaseem, N.; Hajdusek, M.; Vedral, V.; Fazio, R.; Kwek, L.C.; Vinjanampathy, S. Quantum synchronization in nanoscale heat engines. *Phys. Rev. E* **2020**, *101*, 020201. [[CrossRef](#)]
131. Correa, L.A.; Palao, J.P.; Alonso, D. Internal dissipation and heat leaks in quantum thermodynamic cycles. *Phys. Rev. E* **2015**, *92*, 032136. [[CrossRef](#)]
132. Newman, D.; Mintert, F.; Nazir, A. Performance of a quantum heat engine at strong reservoir coupling. *Phys. Rev. E* **2017**, *95*, 032139. [[CrossRef](#)]
133. Perarnau-Llobet, M.; Wilming, H.; Riera, A.; Gallego, R.; Eisert, J. Strong coupling corrections in quantum thermodynamics. *Phys. Rev. Lett.* **2018**, *120*, 120602. [[CrossRef](#)]
134. Shiraishi, N.; Saito, K.; Tasaki, H. Universal trade-off relation between power and efficiency for heat engines. *Phys. Rev. Lett.* **2016**, *117*, 190601. [[CrossRef](#)]
135. Pietzonka, P.; Seifert, U. Universal trade-off between power, efficiency, and constancy in steady-state heat engines. *Phys. Rev. Lett.* **2018**, *120*, 190602. [[CrossRef](#)]
136. Funo, K.; Ueda, M.; Sagawa, T. *Thermodynamics in the Quantum Regime*; Binder, F., Correa, L.A., Gogolin, C., Anders, J., Adesso, G., Eds.; Fundamental Theories of Physics; Springer: Berlin/Heidelberg, Germany, 2018; pp. 249–273. [[CrossRef](#)]
137. Denzler, T.; Lutz, E. Power fluctuations in a finite-time quantum Carnot engine. *arXiv* **2020**, arXiv:2007.01034.
138. Silaev, M.; Heikkilä, T.T.; Virtanen, P. Lindblad-equation approach for the full counting statistics of work and heat in driven quantum systems. *Phys. Rev. E* **2014**, *90*, 022103. [[CrossRef](#)]
139. Tsirlin, A.; Sukin, I. Averaged Optimization and Finite-Time Thermodynamics. *Entropy* **2020**, *22*, 912. [[CrossRef](#)]
140. Tondeur, D.; Kvaalen, E. Equipartition of entropy production. An optimality criterion for transfer and separation processes. *Ind. Eng. Chem. Res.* **1987**, *26*, 50–56. [[CrossRef](#)]
141. Korzekwa, K.; Lostaglio, M.; Oppenheim, J.; Jennings, D. The extraction of work from quantum coherence. *New J. Phys.* **2016**, *18*, 023045. [[CrossRef](#)]
142. Camati, P.A.; Santos, J.F.; Serra, R.M. Coherence effects in the performance of the quantum Otto heat engine. *Phys. Rev. A* **2019**, *99*, 062103. [[CrossRef](#)]
143. Geva, E.; Kosloff, R. On the classical limit of quantum thermodynamics in finite time. *J. Chem. Phys.* **1992**, *97*, 4398–4412. [[CrossRef](#)]
144. Abah, O.; Rossnagel, J.; Jacob, G.; Deffner, S.; Schmidt-Kaler, F.; Singer, K.; Lutz, E. Single-ion heat engine at maximum power. *Phys. Rev. Lett.* **2012**, *109*, 203006. [[CrossRef](#)]
145. Roßnagel, J.; Dawkins, S.T.; Tolazzi, K.N.; Abah, O.; Lutz, E.; Schmidt-Kaler, F.; Singer, K. A single-atom heat engine. *Science* **2016**, *352*, 325–329. [[CrossRef](#)]
146. Abah, O.; Paternostro, M. Shortcut-to-adiabaticity Otto engine: A twist to finite-time thermodynamics. *Phys. Rev. E* **2019**, *99*, 022110. [[CrossRef](#)] [[PubMed](#)]
147. Insinga, A.; Andresen, B.; Salamon, P. Thermodynamical analysis of a quantum heat engine based on harmonic oscillators. *Phys. Rev. E* **2016**, *94*, 012119. [[CrossRef](#)]
148. Insinga, A.; Andresen, B.; Salamon, P.; Kosloff, R. Quantum heat engines: Limit cycles and exceptional points. *Phys. Rev. E* **2018**, *97*, 062153. [[CrossRef](#)]
149. Deffner, S. Efficiency of harmonic quantum Otto engines at maximal power. *Entropy* **2018**, *20*, 875. [[CrossRef](#)]
150. Salamon, P.; Berry, R.S. Thermodynamic length and dissipated availability. *Phys. Rev. Lett.* **1983**, *51*, 1127. [[CrossRef](#)]
151. Peterson, J.P.; Batalhão, T.B.; Herrera, M.; Souza, A.M.; Sarthour, R.S.; Oliveira, I.S.; Serra, R.M. Experimental characterization of a spin quantum heat engine. *arXiv* **2018**, arXiv:1803.06021.
152. Pekola, J.P.; Khaymovich, I.M. Thermodynamics in single-electron circuits and superconducting qubits. *Annu. Rev. Condens. Matter Phys.* **2019**, *10*, 193–212. [[CrossRef](#)]

153. Klatzow, J.; Becker, J.N.; Ledingham, P.M.; Weinzetl, C.; Kaczmarek, K.T.; Saunders, D.J.; Nunn, J.; Walmsley, I.A.; Uzdin, R.; Poem, E. Experimental demonstration of quantum effects in the operation of microscopic heat engines. *Phys. Rev. Lett.* **2019**, *122*, 110601. [[CrossRef](#)]
154. Hofer, P.P.; Brask, J.B.; Perarnau-Llobet, M.; Brunner, N. Quantum thermal machine as a thermometer. *Phys. Rev. Lett.* **2017**, *119*, 090603. [[CrossRef](#)]
155. Bhattacharjee, S.; Bhattacharya, U.; Niedenzu, W.; Mukherjee, V.; Dutta, A. Quantum magnetometry using two-stroke thermal machines. *New J. Phys.* **2020**, *22*, 013024. [[CrossRef](#)]
156. Bhattacharjee, S.; Dutta, A. Quantum thermal machines and batteries. *arXiv* **2020**, arXiv:2008.07889.
157. Levy, A.; Göb, M.; Deng, B.; Singer, K.; Torrontegui, E.; Wang, D. Single-atom heat engine as a sensitive thermal probe. *New J. Phys.* **2020**, *22*, 093020. [[CrossRef](#)]
158. Ronzani, A.; Karimi, B.; Senior, J.; Chang, Y.C.; Peltonen, J.T.; Chen, C.; Pekola, J.P. Tunable photonic heat transport in a quantum heat valve. *Nat. Phys.* **2018**, *14*, 991–995. [[CrossRef](#)]
159. Wei, J.; Norman, E. On global representations of the solutions of linear differential equations as a product of exponentials. *Proc. Am. Math. Soc.* **1964**, *15*, 327–334. [[CrossRef](#)]

Publisher's Note: MDPI stays neutral with regard to jurisdictional claims in published maps and institutional affiliations.



© 2020 by the authors. Licensee MDPI, Basel, Switzerland. This article is an open access article distributed under the terms and conditions of the Creative Commons Attribution (CC BY) license (<http://creativecommons.org/licenses/by/4.0/>).